

# Geophysical Research Letters<sup>®</sup>



## RESEARCH LETTER

10.1029/2023GL103412

### Key Points:

- The Atlantic meridional overturning circulation has been monitored with hydrographic data and now basin-wide arrays enable the detection of high-frequency variability
- Inverse solutions from single sections are affected by aliasing, as they capture the circulation structure of the time of the cruise
- Inverse models with multiple sections at different latitudes and times agree with decadal averages from an ocean general circulation model

### Supporting Information:

Supporting Information may be found in the online version of this article.

### Correspondence to:

V. Caínzos,  
[veronica.cainzos@ulpgc.es](mailto:veronica.cainzos@ulpgc.es)

### Citation:

Caínzos, V., Hernández-Guerra, A., Farneti, R., Pérez-Hernández, M. D., & Talley, L. D. (2023). Mass, heat, and freshwater transport from transoceanic sections in the Atlantic Ocean at 30°S and 24.5°N: Single sections versus box models? *Geophysical Research Letters*, 50, e2023GL103412. <https://doi.org/10.1029/2023GL103412>






Received 23 FEB 2023

Accepted 1 JUN 2023

© 2023 The Authors.

This is an open access article under the terms of the [Creative Commons Attribution-NonCommercial License](https://creativecommons.org/licenses/by-nc/4.0/), which permits use, distribution and reproduction in any medium, provided the original work is properly cited and is not used for commercial purposes.

## Mass, Heat, and Freshwater Transport From Transoceanic Sections in the Atlantic Ocean at 30°S and 24.5°N: Single Sections Versus Box Models?

Verónica Caínzos<sup>1</sup> , Alonso Hernández-Guerra<sup>1</sup> , Riccardo Farneti<sup>2</sup> , M. Dolores Pérez-Hernández<sup>1</sup> , and Lynne D. Talley<sup>3</sup> 

<sup>1</sup>Unidad Océano y Clima, Instituto de Oceanografía y Cambio Global, IOCAG, Universidad de Las Palmas de Gran Canaria, ULPGC, Unidad Asociada ULPGC-CSIC, Canary Islands, Spain, <sup>2</sup>The Abdus Salam International Centre for Theoretical Physics (ICTP), Trieste, Italy, <sup>3</sup>Scripps Institution of Oceanography, University of California San Diego, La Jolla, CA, USA

**Abstract** The Atlantic meridional overturning circulation (AMOC) is central to the climate of the Atlantic by redistributing mass, heat, and freshwater. Hydrographic sections help monitor its strength at different latitudes, and inverse box models provide estimates of AMOC, heat, and freshwater transports. We have used all available hydrographic zonal sections at 24.5°N and 30°S over the last 30 years to conclude that single section inverse models agree with monthly outputs from an ocean general circulation model at the time of the cruise. In contrast, inverse models using multiple sections at different latitudes and times of the year for each of the last three decades are more consistent with decadal averages from the same model. Therefore, solutions of inverse models with single sections are affected by aliasing and represent the state of the ocean at the time of cruise. However, aliasing is greatly reduced when using multiple sections to assess low-frequency variability.

**Plain Language Summary** Heat and nutrients in the Atlantic Ocean are redistributed through a process called Atlantic meridional overturning circulation, which is being monitored to detect changes in its strength. Hydrographic data offer the possibility to assess this variability, although it can be influenced by the ocean dynamics happening at the time of the cruise. When comparing the results from inverse box models applied to single sections with numerical model output, the best fit appears for the time of the cruise. This reflects that the monthly variation affects the solutions of the inverse model, which can be understood as representative of the duration of the cruise. Inverse models using several sections from cruises carried out in different times of the year and different years average out the local temporal phenomena that can affect the results and better represent the decadal average of the numerical models.

## 1. Introduction

The redistribution of heat and the supply of nutrients and carbon into the deep ocean are achieved by the overturning of a northward-flowing upper limb of warm and salty water and a southward lower limb of relatively cold and fresh water (Bower et al., 2019; Srokosz et al., 2012). This process, that extends from the Southern Ocean to the northern North Atlantic, known as the Atlantic Meridional Overturning Circulation (AMOC), is an important factor in climate variability—possible changes in its strength could affect profoundly the climate of maritime and continental Europe (Buckley & Marshall, 2016; Pillar et al., 2016). As a result, there have been numerous efforts to determine the past, present, and future state of the AMOC and its associated transport of mass, heat, and freshwater through the Atlantic (Caesar et al., 2018; Caínzos et al., 2022; Fraser & Cunningham, 2021; Ganachaud & Wunsch, 2000; Lumpkin & Speer, 2007; Macdonald & Wunsch, 1996; Rahmstorf et al., 2015; Talley, 2008).

The AMOC has been quantified with hydrographic data since the 1990s under the World Ocean Circulation Experiment (WOCE) and, later, the GO-SHIP programs (Talley et al., 2016). These programs have allowed to carry out cross-basin zonal sections every 5–10 years enabling the study of the overturning strength at different latitudes and different decades (Bryden et al., 2011; Hernández-Guerra et al., 2014; McDonagh & King, 2005). Hydrographic data provide the opportunity to use observational data that reflect long-term variability of the whole water column.

One of the most used methods to determine circulation from hydrography is inverse modeling (Wunsch, 1996), which has enabled the study and comparison of hydrographic sections conducted at different times (Bryden

et al., 2005; Caínzos et al., 2022; Fu et al., 2018, 2020; Hernández-Guerra et al., 2019; Hernández-Guerra & Talley, 2016; Koltermann et al., 1999). Inverse methods provide an estimation of the absolute geostrophic velocity field of one or several enclosed oceanic boxes bounded by hydrographic sections and ocean boundaries (Wunsch, 1996). They are based on the thermal wind and continuity equations conserving, primarily, mass, but also other properties such as salt, heat or nutrients.

Inverse solutions from single-section snapshots are presumably subject to aliasing (Frajka-Williams et al., 2019; Wunsch & Heimbach, 2006), since they correspond to the time when data are collected. Therefore, the validity of hydrographic data to reconstruct climatological estimates has been debated. Thus, we have focused our efforts in two hydrographic sections, in the North Atlantic at 24.5°N and in the South Atlantic at 30°S, to investigate the significance of the results of inverse models using single sections and verify the aliasing on the data. We have also used results from inverse models applied to multiple sections distributed in space and time to infer their relevance in decadal variations. For this purpose, results from an ocean general circulation model (OGCM) at these latitudes have been compared with the inverse model estimations.

## 2. Data and Methods

In the North Atlantic, the section at 24.5°N (A05) has been occupied repeatedly, as one of the key latitudes monitoring the AMOC. We have selected all seven cruises at 24.5°N, from 1992 to 2020 at different times of the year (Figure 1a). Of all sections, only the 1992 cruise occurred in boreal summer, and 2004 in boreal spring, with the rest sampled during boreal winter (Table S1 in Supporting Information S1). Inverse box models are applied to each single section to calculate the adjusted mass transport per neutral density layer for each pair of stations. The initial choice of the geostrophic reference layer is at the neutral density of 28.15 kg m<sup>-3</sup>, the interphase between the southward North Atlantic Deep Water and the northward Antarctic Bottom Water (Caínzos et al., 2022; Hernández-Guerra et al., 2014, 2019). The inverse model constraints mass transport for the whole section and includes regional constraints using previous measurements at different longitudes and depth ranges as described by Hernández-Guerra et al. (2014). Error estimates are obtained as part of the solution of the inverse model, solved by the Gauss-Markov method. A more in-depth description of configuration of the inverse model appears in Text S1 in Supporting Information S1. After mass transport is adjusted with the inverse model, we estimate both the meridional heat transport (MHT) and meridional freshwater transport (MFT) across the section following Joyce et al. (2001).

Hernández-Guerra et al. (2019) analyzed two different realizations of the South Atlantic subtropical gyre at 30°S (A10), in 2003 and 2011 carried out during austral spring (Figure 2a). For this study, we have also added the previous realization in 1992–1993, sampled in austral summer (Table S1 in Supporting Information S1). The single section inverse models for 30°S apply the same regional constraints as in Hernández-Guerra et al. (2019), described in Text S2 in Supporting Information S1.

Additionally, we have used the results from the inverse models of Caínzos et al. (2022), combining different zonal sections over the Atlantic Ocean carried out in different months and years for each of the last three decades. Originally, only three sections are available at both latitudes, one for each of the last three decades. However, the 24.5°N section has been monitored more regularly and we have been able to obtain seven results using all the sections available. The configuration of the original multiple-section inverse models for 1992, 2004, and 2011 for each of the decades has been applied, maintaining the same configuration so that changes in circulation can be attributed to changes in hydrography. The configuration of these multiple-section inverse models has been summarized in Text S3 in Supporting Information S1.

The Ekman transport is estimated using the National Center for Environmental Prediction and National Center for Atmospheric Research (NCEP–NCAR) surface winds. We compute the Ekman transport for the time of the cruise and include it in the outcropping layers of each section. Hernández-Guerra and Talley (2016) have found no difference between the use of Ekman for the time of the cruise and longer-time averages. The Ekman transport at the time of the cruise is included as part of the initial conditions of the inverse models that then is corrected as part of the inverse solution, yielding an adjustment of the Ekman transport for each section for either single or multiple section models.

Furthermore, we have included the simulation from an OGCM to compare with hydrographic data (Tables S2 and S3 in Supporting Information S1). The OM4 ocean-sea ice model (Adcroft et al., 2019; Tsujino et al., 2020)

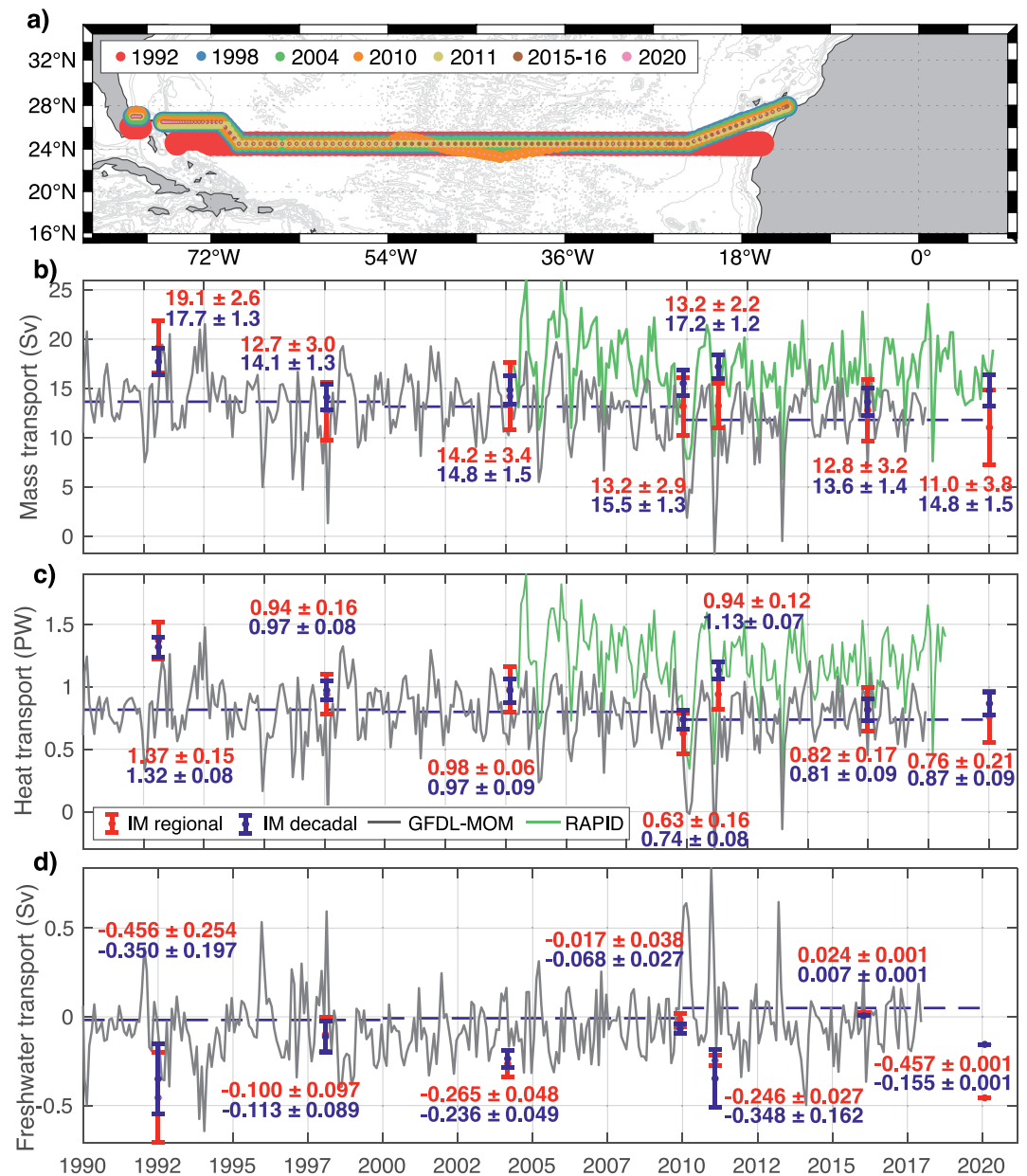


**Figure 1.** Estimates at 24.5°N from inverse solutions and RAPID and GFDL-MOM time series. (a) Map of the zonal sections included at 24.5°N, with station positions for the A05 cruises in 1992, 1998, 2004, 2010, 2011, 2015–2016, and 2020. Monthly time series at 24.5°N (in gray) obtained with GFDL-MOM of (b) Atlantic Meridional Overturning Circulation (AMOC), (c) Meridional Heat Transport (MHT) and (d) Meridional Freshwater Transport. Included in subplots (b–d) appear the estimates from the single-section inverse box models in red, and the decadal estimates following Caínzos et al. (2022) in blue. The decadal averages for 1990–1999, 2000–2009, and 2010–2019 for each estimate appear as the blue dashed lines. AMOC and MHT estimates from the RAPID array time series are shown for comparison in green in subplots (b) and (c), respectively.

developed by the Geophysical Fluid Dynamics Laboratory (GFDL) uses version six of the Modular Ocean Model (GFDL-MOM, hereafter). The simulation follows the OMIP2 protocol and uses the JRA55-do forcing data set v1.4.0 (Tsujino et al., 2018). It is based on the hydrostatic primitive equations formulated in their generalized vertical coordinate form. GFDL-MOM is a free-running model with no data assimilation and a horizontal resolution of 1/4° and 50 vertical levels, providing monthly averages over the 1958–2018 period. Mass, heat, and freshwater transports were computed at 24.5°N and 30°S for the entire simulation, and then integrated over the 11 layers defined by the neutral density interfaces of Hernández-Guerra et al. (2019), the same as used with

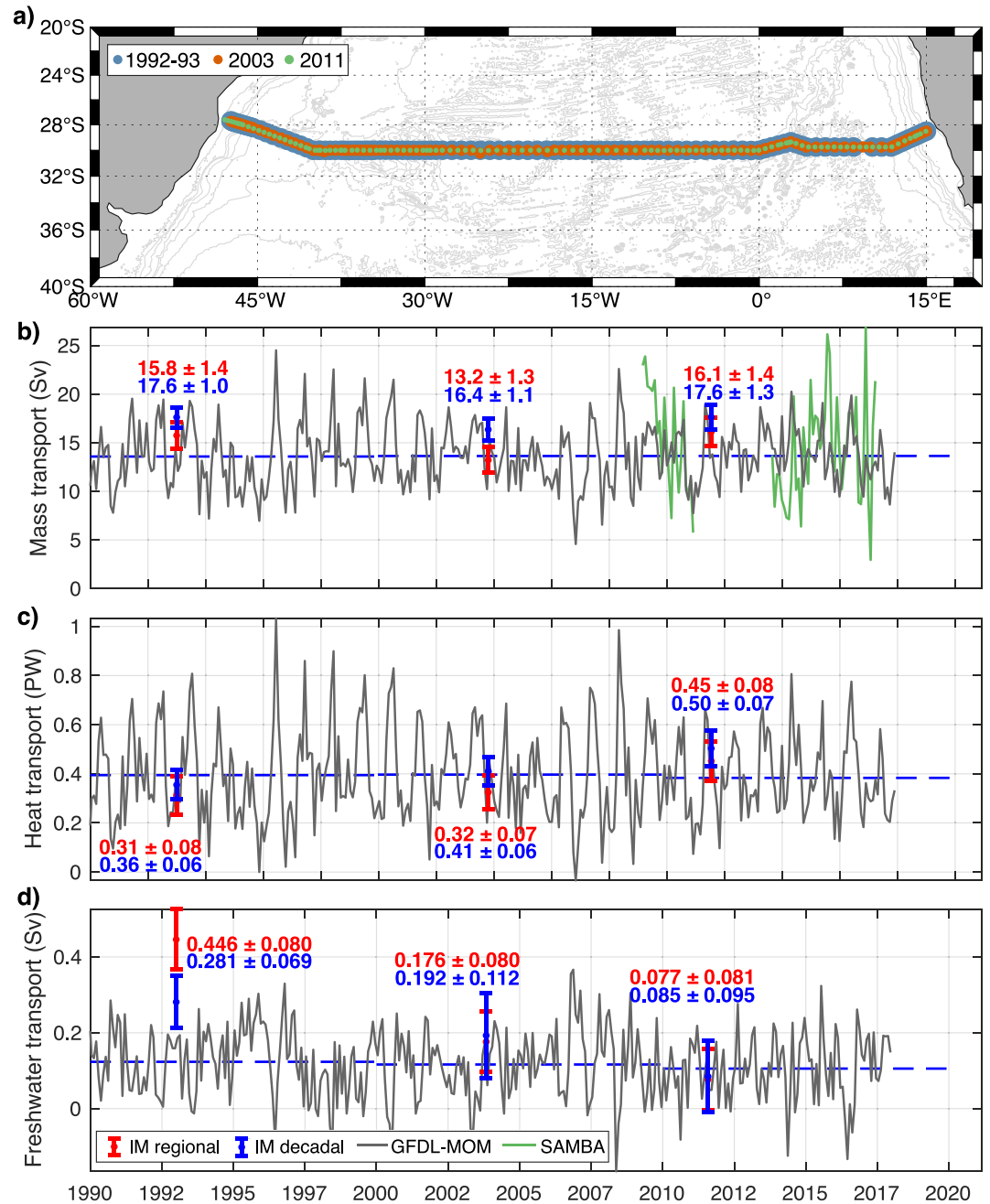


**Figure 2.** Estimates at 30°S from inverse solutions and SAMBA and GFDL-MOM time series. (a) Map of the zonal sections included at 30°S, with station positions for the A10 cruises in 1992–1993, 2003, and 2011. Monthly time series at 30°S (in gray) obtained with GFDL-MOM of (b) Atlantic Meridional Overturning Circulation (AMOC), (c) Meridional Heat Transport and (d) Meridional Freshwater Transport. Included in subplots (b–d) appear the estimates from the single-section inverse box models from Hernández-Guerra et al. (2019) in red, and the decadal estimates following Caínzos et al. (2022) in blue. The decadal averages for 1990–1999, 2000–2009, and 2010–2019 for each estimate appear as the blue dashed lines. AMOC estimates from the SAMBA array time series is shown for comparison in green in subplot (b).

the hydrographic data. Error from the OGCM estimates were computed as the standard error of the mean over the time being averaged. We have chosen the free-running GFDL-MOM model to perform the analysis to prevent finding positive results due to the presence of the observational data used in this study assimilated in the model. The analysis performed with GFDL-MOM has been replicated using two additional OGCMs, described in Text S4 (Figures S1–S4 and Tables S4–S6) in Supporting Information S1.

Moreover, we have used data based, among others, on mooring observations, to validate OGCM solutions. The North Atlantic subtropical gyre at 24.5°N has been closely monitored since the year 2004 with the RAPID/MOCHA/WBTS array (hereafter RAPID; Cunningham et al., 2007; Johns et al., 2011), providing a long-term estimate of the AMOC at this latitude (Figures 1b and 1c). The South Atlantic Meridional Overturning Circulation Basin-wide Array program (hereafter SAMBA; Figure 2b; Kersalé et al., 2020) offers an additional record of the AMOC in the South Atlantic at a latitude close to 30°S (34.5°S).

Finally, to eliminate the impact of the variation in mean strength between observations and numerical models, we have used anomalies. Using the average value for each available cruise realization at each latitude for both inverse models with single and multiple sections, the anomalies for the inverse solutions at 24.5°N and 30°S can be estimated. Inverse models at 24°N yield mean AMOC values of  $13.8 \pm 1.2$  Sv and  $15.4 \pm 0.5$  Sv, mean MHT values of  $0.92 \pm 0.06$  PW and  $0.97 \pm 0.03$  PW, and mean MFT values of  $-0.217 \pm 0.041$  Sv and  $-0.180 \pm 0.039$  Sv with single and multiple sections, respectively. At 30°S, the AMOC mean values are  $15.0 \pm 0.3$  Sv and  $17.2 \pm 0.3$  Sv, the mean MHT are  $0.36 \pm 0.02$  PW and  $0.42 \pm 0.02$  PW, and the mean MFT are  $0.233 \pm 0.020$  Sv and  $0.186 \pm 0.023$  Sv for inverse solutions from single sections and from a combination of multiple sections, respectively. The anomalies for GFDL-MOM for both sections are computed by subtracting the average value for the whole time series (13.0 Sv for AMOC, 0.79 PW for MHT, and  $-0.062$  Sv for MFT at 24.5°N and 13.6 Sv for AMOC, 0.39 PW for MHT, and 0.116 Sv for MFT at 30°S). Lastly, the anomalies for RAPID and SAMBA were computed similarly to GFDL-MOM, yielding mean values of 16.9 Sv for AMOC and 1.20 PW for MHT for RAPID and 14.6 Sv for the SAMBA AMOC.

### 3. Results

#### 3.1. Meridional Overturning Circulation From Single Sections

The strength of the AMOC is computed as the maximum in the zonally integrated and vertically accumulated mass transport. We have studied the intensity of the AMOC at 24.5°N and 30°S for the last 30 years using the available hydrographic data, GFDL-MOM values and mooring arrays (Figures 1b and 2b).

The hydrographic section at 24.5°N has been occupied on seven occasions (Figure 1). The inverse solutions from individual sections present similar values of the AMOC except for the first cruise, with estimates of  $19.1 \pm 2.6$ ,  $12.7 \pm 3.0$ ,  $14.2 \pm 3.4$ ,  $13.2 \pm 2.9$ ,  $13.2 \pm 2.2$ ,  $12.8 \pm 3.2$ , and  $11.0 \pm 3.8$  Sv for the 1992, 1998, 2004, 2010, 2011, 2015–2016, and 2020 cruises, respectively (Table S2 in Supporting Information S1). On the other hand, we have validated the AMOC time series from GFDL-MOM with the estimates from the RAPID array. The absolute values present differences in their mean value (16.9 and 13.0 Sv for RAPID and GFDL-MOM, respectively), with a Root Mean Squared Error (RMSE) of 5.2 Sv. However, when comparing the anomalies, the variability agrees over the period 2004–2020 with a reduced RMSE of 2.4 Sv, lower than their standard deviations (3.4 and 3.3 Sv for RAPID and GFDL-MOM), and an  $R^2$  correlation of 0.6 (Figure 1b, green and gray lines). To compute the agreement on interannual time scales, we have applied a low-pass Butterworth filter with a 1-year cut-off period for both RAPID and GFDL-MOM (Figure S5 in Supporting Information S1). For these filtered signals we have also obtained relatively large values of  $R^2$  of 0.7.

In the South Atlantic, all three computations of AMOC from hydrographic data at 30°S present relatively similar inverse solutions (Table S2 in Supporting Information S1), with values of  $15.8 \pm 1.3$ ,  $13.2 \pm 1.3$ , and  $16.1 \pm 1.4$  Sv for the 1992–1993, 2003, and 2011 cruises, respectively. We have also used the nearby SAMBA array at 34.5°S to validate the data from GFDL-MOM in the South Atlantic at 34.5°S. When comparing the absolute values of SAMBA (standard deviation of 5.4 Sv) with GFDL-MOM at 34.5°S (standard deviation of 3.1 Sv) we find a RMSE of 5.4 Sv that is not greatly reduced when using the anomalies (RMSE of 5.2 Sv) with a low  $R^2$  of 0.1 (Figure S6b in Supporting Information S1, green and gray lines).

We have compared the AMOC anomalies from these single-section inverse models with the GFDL-MOM continuous time series at both latitudes (Table 1). At 24.5°N, the comparison yields RMSE values of 1.8 Sv for the anomaly estimates for the time of the cruise and 2.4 Sv for the decadal GFDL-MOM anomalies, both lower than the standard deviation for GFDL-MOM (3.3 Sv). At 30°S, GFDL-MOM estimates show a good agreement with the inverse solutions for the time of the cruise with a RMSE of 0.9 Sv, and a higher RMSE of 1.4 Sv for the decadal anomalies, again lower than GFDL-MOM standard deviation (3.2 Sv). Thus, in both cases, the RMSE for decadal averages are larger than for the values at the time of the cruise, indicating that the decadal averages offer

**Table 1**

*Root Mean Squared Errors (RMSE) for 24.5°N and 30°S for the Anomalies of Atlantic Meridional Overturning Circulation (AMOC, in Sv), Meridional Heat Transport (MHT, in PW) and Meridional Freshwater Transport (MFT, in Sv) Comparing the Values From the Single-Section Inverse Models of This Study and the Multiple-Section Inverse Model Solutions as in Caínzos et al. (2022) With GFDL-MOM Values for Both the Time of the Cruise and the Decadal Averages*

		GFDL-MOM cruise	GFDL-MOM decadal
24.5°N			
Single-section inverse model	RMSE AMOC (Sv)	<b>1.8</b>	2.4
	RMSE MHT (PW)	<b>0.18</b>	0.19
	RMSE MFT (Sv)	<b>0.220</b>	0.280
Multiple-section inverse model	RMSE AMOC (Sv)	3.9	<b>1.5</b>
	RMSE MHT (PW)	0.19	<b>0.15</b>
	RMSE MFT (Sv)	0.277	<b>0.267</b>
30°S			
Single-section inverse model	RMSE AMOC (Sv)	<b>0.9</b>	1.4
	RMSE MHT (PW)	<b>0.05</b>	0.07
	RMSE MFT (Sv)	<b>0.180</b>	0.193
Multiple-section inverse model	RMSE AMOC (Sv)	2.9	<b>2.6</b>
	RMSE MHT (PW)	0.09	<b>0.07</b>
	RMSE MFT (Sv)	<b>0.084</b>	0.104

*Note.* For reference, at 24.5°N, GFDL-MOM presents a standard deviation of 3.3 Sv for AMOC, 0.24 PW for MHT and 0.202 Sv for MFT. At 30°S, the standard deviations for AMOC, MHT, and MFT are, respectively, 3.2 Sv, 0.18 PW, and 0.093 Sv. Lower values of RMSE appear in bold.

worse results than the estimates at the time of the cruise as obtained by Atkinson et al. (2012), Frajka-Williams et al. (2019), and Wunsch and Heimbach (2006). Similar results appear when comparing with data-assimilating OGCMs (Figures S1–S4 and Tables S4–S6 in Supporting Information S1).

### 3.2. Meridional Heat Transport From Single Sections

The radiative heating from the sun, absorbed mainly in the tropics, is redistributed along the Atlantic. In general, the net northward MHT presents higher values closer to the equator (Caínzos et al., 2022), with a large part of the heat transport due to its baroclinic component, that comprises the zonally averaged meridional circulation (Bryden & Imawaki, 2001).

The MHT for each cruise carried out at 24.5°N are  $1.37 \pm 0.15$ ,  $0.94 \pm 0.16$ ,  $0.98 \pm 0.19$ ,  $0.63 \pm 0.16$ ,  $0.94 \pm 0.12$ ,  $0.82 \pm 0.17$ ,  $0.76 \pm 0.21$  PW for the 1992, 1998, 2004, 2010, 2011, 2015–2016, and 2020 cruises, respectively (Table S2 in Supporting Information S1). Similar to the AMOC, the RAPID array monitors the variability of MHT at 24.5°N (Bryden et al., 2020; Johns et al., 2011; McCarthy et al., 2015), with an average of 1.19 PW and a standard deviation of 0.27 PW for the period 2004–2018 (Figure 1c). The comparison between GFDL-MOM estimations and the RAPID values yields RMSE of 0.5 PW for the absolute values, with a reduced error when using anomalies (RMSE of 0.2 PW), in the order of their standard deviations (0.27 PW for RAPID and 0.24 PW for GFDL-MOM). The correlation between GFDL-MOM and RAPID MHT anomalies is relatively strong, as expected from the high correlation in AMOC, with an  $R^2$  of 0.7.

The average net heat transport across 30°S for the whole water column is  $0.31 \pm 0.08$ ,  $0.32 \pm 0.07$ ,  $0.45 \pm 0.08$  PW for the 1992–1993, 2003, and 2011 cruises, respectively (Table S2 in Supporting Information S1). Unfortunately, no values of MHT are available for comparison between GFDL-MOM and the SAMBA array (Figure 2c) as carried out at 24.5°N.

Analogously to AMOC, we have compared the single section inverse model results to the GFDL-MOM estimates of MHT anomalies for the time of the cruise and for decadal averages (Table 1). At 24.5°N, we find slightly lower values of RMSE for the time of the cruise estimates than for decadal averages (0.18 and 0.19 PW, respectively)

both in the range of standard deviation for GFDL-MOM (0.24 PW). Similarly, at 30°S, the time of cruise estimates from GFDL-MOM MHT anomalies have an RMSE of 0.05 PW, lower than the 0.07 PW of decadal averages. Both these values are included in the standard deviation for GFDL-MOM (0.18 PW). Therefore, as for AMOC, the inverse solutions from single sections are closer to the values at the time of the cruise than the decadal averages.

### 3.3. Meridional Freshwater Transport From Single Sections

The freshwater flux can be understood as the non-salt part of the mass transport (McDonagh et al., 2015) resulting from the balance between precipitation, evaporation and river runoff (Figures 1d and 2d). At 24.5°N, the solutions from the inverse box models are  $-0.456 \pm 0.254$ ,  $-0.100 \pm 0.097$ ,  $-0.265 \pm 0.048$ ,  $-0.017 \pm 0.038$ ,  $-0.246 \pm 0.027$ ,  $0.024 \pm 0.001$ , and  $-0.457 \pm 0.001$  Sv for the 1992, 1998, 2004, 2010, 2011, 2015–2016, and 2020 cruises, respectively. The inverse solutions of MFT for 30°S are  $0.446 \pm 0.080$ ,  $0.176 \pm 0.080$ , and  $0.077 \pm 0.081$  Sv for the 1992–1993, 2003, and 2011 cruises, respectively (Table S2 in Supporting Information S1).

We have also compared the MFT anomaly estimates from the single-section inverse models with the GFDL-MOM anomaly estimates for the time of the cruise and the decadal averages (Table 1). As for AMOC and MHT, lower RMSE appears when comparing with the time of the cruise (0.220 Sv at 24.5°N and 0.180 Sv at 30°S) than with the decadal averages (0.280 Sv at 24.5°N and 0.193 Sv at 30°S). At 24.5°N, the standard deviation of GFDL-MOM (0.202 Sv) is larger than the RMSE values, while at 30°S the standard deviation is lower (0.093 Sv).

### 3.4. Comparison With Decadal Values Using Multiple Section Inverse Models

Caínzos et al. (2022) have already estimated the AMOC, MHT, and MFT for 24.5°N and 30°S with an inverse model spanning the whole Atlantic Ocean basin with sections carried out in different years within the decades 1990–1999, 2000–2009, and 2010–2019. We have compared these estimates with GFDL-MOM values at the time of the cruise and decadal averages for AMOC, MHT, and MFT, to check whether solutions from several sections yield different results than those from single section inverse box models (Table 1).

At 24.5°N, the AMOC estimates from multiple sections are  $17.7 \pm 1.3$ ,  $14.1 \pm 1.3$ ,  $14.8 \pm 1.5$ ,  $15.5 \pm 1.3$ ,  $17.2 \pm 1.2$ ,  $13.6 \pm 1.4$ , and  $14.8 \pm 1.5$  Sv, for the 1990–1999, 2000–2009, and 2010–2019 decades using the 1992, 1998, 2004, 2010, 2011, 2015–2016, and 2020 sections, respectively (Table S3 in Supporting Information S1). These values present a lower RMSE when comparing with GFDL-MOM estimates of AMOC anomaly for the decadal averages (1.5 Sv) than for the time of the cruise (3.9 Sv), thus indicating that the solutions from Caínzos et al. (2022) are better represented by GFDL-MOM decadal averages.

The relatively stable results of AMOC from Caínzos et al. (2022) of  $17.6 \pm 1.0$ ,  $16.4 \pm 1.1$ , and  $17.6 \pm 1.3$  Sv for 1990–1999, 2000–2009, and 2010–2019, respectively (Table S3 in Supporting Information S1), appear also for GFDL-MOM at 30°S. Thus, the multiple-section inverse solutions from Caínzos et al. (2022) are better represented by the GFDL-MOM decadal averages of AMOC anomalies (RMSE of 2.6 Sv) than by the time of the cruise values from GFDL-MOM (RMSE of 2.9 Sv).

MHT displays a similar behavior to AMOC (Table S3 in Supporting Information S1), with lower RMSE (Table 1) when comparing MHT anomaly estimates from multiple sections and GFDL-MOM for the decadal averages (0.15 PW at 24.5°N and 0.07 PW at 30°S) than for the time of the cruise (0.19 PW at 24.5°N and 0.09 PW at 30°S).

MFT presents contradicting results between both latitudes (Table 1; Table S3 in Supporting Information S1). At 24.5°N, MFT anomaly estimates from multiple-section inverse models are in better agreement with the decadal averages from GFDL-MOM (RMSE of 0.267 Sv) than with the values for the time of the cruise (RMSE of 0.277 Sv). Nonetheless, at 30°S lower RMSE appear when comparing the solutions from the inverse models with GFDL-MOM estimates for the time of the cruise (0.084 Sv) than with decadal averages (0.104 Sv).

## 4. Discussion and Conclusions

An enormous amount of effort has gone into comprehending the variability of the AMOC on various timescales, appearing mostly on timescales from seasonal, intra-annual, interannual to decadal. The mechanisms underlying

these variations are highly dependent on the region of study. In the subtropics, wind forcing dominates AMOC variability at higher frequencies, with contributions from buoyancy forcing at lower frequencies. The subpolar North Atlantic, in contrast, is dominated by low-frequency variability forced by buoyancy and wind. Both modes of variation of the AMOC are linked to the North Atlantic Oscillation, which is the main source of atmospheric variability in the North Atlantic (Jackson et al., 2022; Johnson et al., 2019).

The timescales and meridional coherence of AMOC variability are still up to debate. Observations have consistently found no significant trends for the AMOC over long timescales (Caínzos et al., 2022; Fu et al., 2020; Le Bras et al., 2023; Worthington et al., 2021), marking the disconnection with results from model projections and proxy reconstructions. Using ensembles of coupled models from CMIP5 and CMIP6, Weijer et al. (2020) have found a consistent decline in the strength of the AMOC over the 21st century in response to anthropogenic climate change. However, this AMOC simulation can be affected by model biases due to misrepresentation of processes such as mixing by mesoscale eddies, transports in narrow boundary currents, mixing in overflows, deep convection, and atmosphere–ocean feedbacks.

This study can be considered as a valuable assessment for developing inverse box models using hydrographic sections, which is one of the few approaches available to estimate ocean circulation. However, we cannot assume that the estimations from inverse models correspond to the time-average values. Several studies have understood inverse solutions obtained from hydrographic sections as snapshots of the circulation at the time of the cruise. We have been working on understanding the adjustment of the inverse model on the use of single or multiple sections, and whether those solutions can represent the time of the cruise or a longer period. As we have seen in the results from single-section inverse models, hydrographic data from a single section captures the variability at the time of the cruise. Thus, the circulation obtained from these models represent the seasonal variability.

We have first compared the AMOC solutions from inverse box models of single sections at two key latitudes (24.5°N and 30°S) in the Atlantic Ocean with estimations from GFDL-MOM for the last 30 years. However, the availability of only three surveys at 30°S result in less meaningful statistics, which is also true for multiple-section inverse solutions.

Concurrently, at 24.5°N, we have validated AMOC and MHT from GFDL-MOM estimations against the continuous measurements of the RAPID array from 2004 to 2019, finding a good agreement between them in terms of anomalies. At 30°S we have used the available AMOC time series from the SAMBA array at the close latitude of 34.5°S, yielding lower convincing results than at 24.5°N, presumably due to the different latitudes in both measurements.

The comparison of AMOC, MHT, and MFT between single section inverse solutions and estimates for the time of the cruise from GFDL-MOM provides consistent results, depicted by the lower RMSE values (1.8 Sv, 0.18 PW and 0.220 Sv at 24.5°N and 0.9 Sv, 0.05 PW and 0.180 Sv at 30°S for AMOC, MHT, and MFT anomalies, respectively) than for the GFDL-MOM decadal estimations (Table 1). Furthermore, when comparing inverse solutions from combinations of multiple hydrographic sections carried out in different seasons and years, GFDL-MOM decadal averages result in a better agreement (1.5 Sv and 0.15 PW at 24.5°N and 2.6 Sv and 0.07 PW at 30°S for AMOC anomalies) than using values for the time of the cruise (3.9 Sv and 0.19 PW at 24.5°N and 2.9 Sv and 0.09 PW at 30°S).

Differences in inverse box model solutions emerge at both latitudes depending on whether single or multiple sections are used (Tables S2 and S3 in Supporting Information S1). The inverse model estimates the velocity at the reference level for each pair of stations from the equations specified in the model. In a single section, the continuity equation applies only to the net transport across the section. However, for box models with several sections, the continuity equation applies to the box specified by different sections, establishing a relationship between the transport of water advected from one section to the next, for the whole column and for each of the layers in which the water column is divided. As a result, there is an influence of one section onto the other and vice versa, forcing the model to adjust the velocities at the reference level at each section to a solution that satisfies all the conditions applied to all sections. By creating a composite of multiple sections, no single section is representative of the year/month when sampled and, thus, is more representative of the mean circulation (Ganachaud & Wunsch, 2000; Lumpkin & Speer, 2007; Macdonald & Wunsch, 1996; Reid, 1989, 1994).

### Data Availability Statement

Hydrographic data were collected from the CCHDO website (<https://cchdo.ucsd.edu>) in the frame of International WOCE and GO-SHIP projects for each cruise: A10 1993 ([https://cchdo.ucsd.edu/cruise/06MT22\\_5](https://cchdo.ucsd.edu/cruise/06MT22_5)), A10 2003 (<https://cchdo.ucsd.edu/cruise/49NZ20031106>), A10 2011 (<https://cchdo.ucsd.edu/cruise/33RO20110926>),



A05 1992 ([https://cchdo.ucsd.edu/cruise/29HE06\\_1](https://cchdo.ucsd.edu/cruise/29HE06_1)), A05 1998 ([https://cchdo.ucsd.edu/cruise/31R-BOACES24N\\_2](https://cchdo.ucsd.edu/cruise/31R-BOACES24N_2)), A05 2004 (<https://cchdo.ucsd.edu/cruise/74DI20040404>), A05 2010 (<https://cchdo.ucsd.edu/cruise/74DI20100106>), A05 2011 (<https://cchdo.ucsd.edu/cruise/29AH20110128>), A05 2015 (<https://cchdo.ucsd.edu/cruise/74EQ20151206>), and A05 2020 (<https://cchdo.ucsd.edu/cruise/740H20200119>). The Florida Current cable and section data are made freely available on the Atlantic Oceanographic and Meteorological Laboratory web page ([www.aoml.noaa.gov/phod/floridacurrent/](http://www.aoml.noaa.gov/phod/floridacurrent/)) and are funded by the DOC-NOAA Climate Program Office—Ocean Observing and Monitoring Division. Florida Current daily mean transport from year 2000 until present is available at [https://www.aoml.noaa.gov/phod/floridacurrent/data\\_access.php](https://www.aoml.noaa.gov/phod/floridacurrent/data_access.php) and historical data from 1982 to 1998 at [https://www.aoml.noaa.gov/phod/floridacurrent/historical\\_data.php](https://www.aoml.noaa.gov/phod/floridacurrent/historical_data.php), of which we have used the used data from 1990 to 1998. The daily mean  $u$  and  $v$ -wind components of NCEP/NCAR reanalysis winds were collected from <https://psl.noaa.gov/data/gridded/data.ncep.reanalysis.pressure.html>. MOM model is a free software distributed under GPLv2 and is part of an open-source community. A central repository is hosted on GitHub (<https://github.com/NOAA-GFDL/MOM6>). ECCO data were obtained as part of the work of ECCO Consortium, Fukumori, I., Wang, O., Fenty, I., Forget, G., Heimbach, P., and Ponte, R. M. (13 May 2021), ECCO Central Estimate (Version 4 Release 4). Retrieved from <https://ecco-group.org/products-ECCO-V4r4.htm>. GLORYS global ocean model outputs were provided by the Copernicus Marine Environment Monitoring Service (CMEMS) (<http://marine.copernicus.eu/services-portfolio/access-to-products/>). Data from the RAPID-MOCHA program are funded by the U.S. National Science Foundation and UK Natural Environment Research Council. AMOC data from the RAPID-MOCHA are freely available at [https://rapid.ac.uk/rapidmoc/rapid\\_data/data\\_dl.php](https://rapid.ac.uk/rapidmoc/rapid_data/data_dl.php) (<https://doi.org/10/d3z4>) and heat transports at <https://mocha.rsmas.miami.edu/mocha/results/index.html> (<https://doi.org/10/gwqg>). The SAMOC International web page hosts the MOC and MHT values from Meinen et al. (2018) at [https://www.aoml.noaa.gov/phod/SAMOC\\_international/documents/MOC\\_TotalAnomaly\\_and\\_constituents.asc](https://www.aoml.noaa.gov/phod/SAMOC_international/documents/MOC_TotalAnomaly_and_constituents.asc).

#### Acknowledgments

We thank the chief scientists and teams that collected all the data for the zonal sections of A10 at 30°S: T. Müller, Y. Yoshikawa, M. Baringer and A. Macdonald. And for the zonal sections of A05 at 24.5°N: G. Parrilla, D. S. Bitterman, K. Lee, S. Cunningham, B. A. King, and A. Sánchez-Franks. V.C. acknowledges the Agencia Canaria de Investigación, Innovación y Sociedad de la Información (ACIISI) grant program of “Apoyo al personal investigador en formación” TESIS2019010015. This study was supported by the SAGA project (RTI2018-100844-B-C31) funded by the Ministerio de Ciencia, Innovación y Universidades of the Spanish Government.

#### References

- Adcroft, A., Anderson, W., Balaji, V., Blanton, C., Bushuk, M., Dufour, C. O., et al. (2019). The GFDL global ocean and sea ice model OM4.0: Model description and simulation features. *Journal of Advances in Modeling Earth Systems*, *11*(10), 3167–3211. <https://doi.org/10.1029/2019MS001726>
- Atkinson, C. P., Bryden, H. L., Cunningham, S. A., & King, B. A. (2012). Atlantic transport variability at 25°N in six hydrographic sections. *Ocean Science*, *8*(4), 497–523. <https://doi.org/10.5194/os-8-497-2012>
- Bower, A., Lozier, S., Biastoch, A., Drouin, K., Foukal, N., Furey, H., et al. (2019). Lagrangian views of the pathways of the Atlantic Meridional Overturning Circulation. *Journal of Geophysical Research: Oceans*, *124*(8), 5313–5335. <https://doi.org/10.1029/2019JC015014>
- Bryden, H. L., & Imawaki, S. (2001). Chapter 6.1 Ocean heat transport. In G. Siedler, J. Church, & J. Gould (Eds.), *Ocean circulation & climate: Observing and modelling the global ocean* (pp. 455–474). Academic Press. [https://doi.org/10.1016/S0074-6142\(01\)80134-0](https://doi.org/10.1016/S0074-6142(01)80134-0)
- Bryden, H. L., Johns, W. E., King, B. A., McCarthy, G., McDonagh, E. L., Moat, B. I., & Smeed, D. A. (2020). Reduction in ocean heat transport at 26°N since 2008 cools the eastern subpolar gyre of the North Atlantic Ocean. *Journal of Climate*, *33*(5), 1677–1689. <https://doi.org/10.1175/JCLI-D-19-0323.1>
- Bryden, H. L., King, B. A., & McCarthy, G. D. (2011). South Atlantic overturning circulation at 24°S. *Journal of Marine Research*, *69*(1), 39–56. <https://doi.org/10.1357/002224011798147633>
- Bryden, H. L., Longworth, H. R., & Cunningham, S. A. (2005). Slowing of the Atlantic meridional overturning circulation at 25°N. *Nature*, *438*(7068), 655–657. <https://doi.org/10.1038/nature04385>
- Buckley, M. W., & Marshall, J. (2016). Observations, inferences, and mechanisms of the Atlantic Meridional Overturning Circulation: A review. *Reviews of Geophysics*, *54*(1), 5–63. <https://doi.org/10.1002/2015RG000493>
- Caesar, L., Rahmstorf, S., Robinson, A., Feulner, G., & Saba, V. (2018). Observed fingerprint of a weakening Atlantic Ocean overturning circulation. *Nature*, *556*(7700), 191–196. <https://doi.org/10.1038/s41586-018-0006-5>
- Caínzos, V., Hernández-Guerra, A., McCarthy, G. D., McDonagh, E. L., Cubas Armas, M., & Pérez-Hernández, M. D. (2022). Thirty years of GOSHIP and WOCE data: Atlantic overturning of mass, heat, and freshwater transport. *Geophysical Research Letters*, *49*(4). <https://doi.org/10.1029/2021GL096527>
- Cunningham, S. A., Kanzow, T., Rayner, D., Baringer, M. O., Johns, W. E., Marotzke, J., et al. (2007). Temporal variability of the Atlantic meridional overturning circulation at 26.5°N. *Science*, *317*(5840), 935–938. <https://doi.org/10.1126/science.1141304>
- Frajka-Williams, E., Anson, I. J., Baehr, J., Bryden, H. L., Chidichimo, M. P., Cunningham, S. A., et al. (2019). Atlantic meridional overturning circulation: Observed transport and variability. *Frontiers in Marine Science*, *6*(260). <https://doi.org/10.3389/fmars.2019.00260>
- Fraser, N. J., & Cunningham, S. A. (2021). 120 years of AMOC variability reconstructed from observations using the Bernoulli inverse. *Geophysical Research Letters*, *48*(18). <https://doi.org/10.1029/2021GL093893>
- Fu, Y., Karstensen, J., & Brandt, P. (2018). Atlantic Meridional Overturning Circulation at 14.5°N in 1989 and 2013 and 24.5°N in 1992 and 2015: Volume, heat, and freshwater transports. *Ocean Science*, *14*(4), 589–616. <https://doi.org/10.5194/os-14-589-2018>
- Fu, Y., Li, F., Karstensen, J., & Wang, C. (2020). A stable Atlantic Meridional Overturning Circulation in a changing North Atlantic Ocean since the 1990s. *Science Advances*, *6*(48), eabc7836. <https://doi.org/10.1126/sciadv.abc7836>
- Ganachaud, A. S., & Wunsch, C. (2000). Improved estimates of global ocean circulation, heat transport and mixing from hydrographic data. *Nature*, *408*(6811), 453–456. <https://doi.org/10.1038/35044048>
- Hernández-Guerra, A., Pelegrí, J. L., Fraile-Nuez, E., Benítez-Barrios, V. M., Emelianov, M., Pérez-Hernández, M. D., et al. (2014). Meridional overturning transports at 7.5N and 24.5N in the Atlantic Ocean during 1992–93 and 2010–11. *Progress in Oceanography*, *128*, 98–114. <https://doi.org/10.1016/j.pocean.2014.08.016>

- Hernández-Guerra, A., & Talley, L. D. (2016). Meridional overturning transports at 30°S in the Indian and Pacific Oceans in 2002–2003 and 2009. *Progress in Oceanography*, 146, 89–120. <https://doi.org/10.1016/j.pocean.2016.06.005>
- Hernández-Guerra, A., Talley, L. D., Pelegrí, J. L., Vélez-Belchí, P., Baringer, M. O., Macdonald, A. M., & McDonagh, E. L. (2019). The upper, deep, abyssal and overturning circulation in the Atlantic Ocean at 30°S in 2003 and 2011. *Progress in Oceanography*, 176, 102136. <https://doi.org/10.1016/j.pocean.2019.102136>
- Jackson, L. C., Biastoch, A., Buckley, M. W., Desbruyères, D. G., Frajka-Williams, E., Moat, B., & Robson, J. (2022). The evolution of the North Atlantic Meridional Overturning Circulation since 1980. *Nature Reviews Earth & Environment*, 3(4), 0123456789. <https://doi.org/10.1038/s43017-022-00263-2>
- Johns, W. E., Baringer, M. O., Beal, L. M., Cunningham, S. A., Kanzow, T., Bryden, H. L., et al. (2011). Continuous, array-based estimates of Atlantic Ocean heat transport at 26.5°N. *Journal of Climate*, 24(10), 2429–2449. <https://doi.org/10.1175/2010JCLI3997.1>
- Johnson, H. L., Cessi, P., Marshall, D. P., Schloesser, F., & Spall, M. A. (2019). Recent contributions of theory to our understanding of the Atlantic Meridional Overturning Circulation. *Journal of Geophysical Research: Oceans*, 124(8), 1–24. <https://doi.org/10.1029/2019jc015330>
- Joyce, T. M., Hernández-Guerra, A., & Smethie, W. M. (2001). Zonal circulation in the NW Atlantic and Caribbean from a meridional World Ocean Circulation Experiment hydrographic section at 66°W. *Journal of Geophysical Research*, 106(C10), 22095–22113. <https://doi.org/10.1029/2000jc000268>
- Kersalé, M., Meinen, C. S., Perez, R. C., le Hénaff, M., Valla, D., Lamont, T., et al. (2020). Highly variable upper and abyssal overturning cells in the South Atlantic. *Science Advances*, 6(32), eaba7573. <https://doi.org/10.1126/sciadv.aba7573>
- Koltermann, K. P., Sokov, A. v., Tereshchenkov, V. P., Dobroliubov, S. A., Lorbacher, K., & Sy, A. (1999). Decadal changes in the thermohaline circulation of the North Atlantic. *Deep-Sea Research Part II: Topical Studies in Oceanography*, 46(1–2), 109–138. [https://doi.org/10.1016/S0967-0645\(98\)00115-5](https://doi.org/10.1016/S0967-0645(98)00115-5)
- Le Bras, I. A., Willis, J., & Fenty, I. (2023). The Atlantic Meridional Overturning Circulation at 35°N from deep moorings, floats, and satellite altimeter. *Geophysical Research Letters*, 50(10), 1–10. <https://doi.org/10.1029/2022GL101931>
- Lumpkin, R., & Speer, K. G. (2007). Global ocean meridional overturning. *Journal of Physical Oceanography*, 37(10), 2550–2562. <https://doi.org/10.1175/jpo3130.1>
- Macdonald, A. M., & Wunsch, C. (1996). An estimate of global ocean circulation and heat fluxes. *Nature*, 382(6590), 436–439. <https://doi.org/10.1038/382436a0>
- McCarthy, G. D., Haigh, I. D., Hirschi, J. J. M., Grist, J. P., & Smeed, D. A. (2015). Ocean impact on decadal Atlantic climate variability revealed by sea-level observations. *Nature*, 521(7553), 508–510. <https://doi.org/10.1038/nature14491>
- McDonagh, E. L., & King, B. A. (2005). Oceanic fluxes in the South Atlantic. *Journal of Physical Oceanography*, 35(1), 109–122. <https://doi.org/10.1175/JPO-2666.1>
- McDonagh, E. L., King, B. A., Bryden, H. L., Courtois, P., Szuts, Z., Baringer, M. O., et al. (2015). Continuous estimate of Atlantic oceanic freshwater flux at 26.5°N. *Journal of Climate*, 28(22), 8888–8906. <https://doi.org/10.1175/jcli-d-14-00519.1>
- Meinen, C. S., Speich, S., Piola, A. R., Ansorge, I., Campos, E., Kersalé, M., et al. (2018). Meridional overturning circulation transport variability at 34.5°S during 2009–2017: Baroclinic and barotropic flows and the dueling influence of the boundaries. *Geophysical Research Letters*, 45(9), 4180–4188. <https://doi.org/10.1029/2018GL077408>
- Pillar, H. R., Heimbach, P., Johnson, H. L., & Marshall, D. P. (2016). Dynamical attribution of recent variability in Atlantic Overturning. *Journal of Climate*, 29(9), 3339–3352. <https://doi.org/10.1175/JCLI-D-15-0727.1>
- Rahmstorf, S., Box, J. E., Feulner, G., Mann, M. E., Robinson, A., Rutherford, S., & Schaffernicht, E. J. (2015). Exceptional twentieth-century slowdown in Atlantic Ocean overturning circulation. *Nature Climate Change*, 5(5), 475–480. <https://doi.org/10.1038/nclimate2554>
- Reid, J. L. (1989). On the total geostrophic circulation of the South Atlantic Ocean: Flow patterns, tracers and transports. *Progress in Oceanography*, 23(3), 149–244. [https://doi.org/10.1016/0079-6611\(89\)90001-3](https://doi.org/10.1016/0079-6611(89)90001-3)
- Reid, J. L. (1994). On the total geostrophic circulation of the North Atlantic Ocean: Flow patterns, tracers and transports. *Progress in Oceanography*, 33, 1–92. [https://doi.org/10.1016/0079-6611\(94\)90014-0](https://doi.org/10.1016/0079-6611(94)90014-0)
- Srokosz, M., Baringer, M., Bryden, H., Cunningham, S., Delworth, T., Lozier, S., et al. (2012). Past, present, and future changes in the Atlantic Meridional Overturning Circulation. *Bulletin of the American Meteorological Society*, 93(11), 1663–1676. <https://doi.org/10.1175/BAMS-D-11-00151.1>
- Talley, L. D. (2008). Freshwater transport estimates and the global overturning circulation: Shallow, deep and throughflow components. *Progress in Oceanography*, 78(4), 257–303. <https://doi.org/10.1016/j.pocean.2008.05.001>
- Talley, L. D., Feely, R. A., Sloyan, B. M., Wanninkhof, R., Baringer, M. O., Bullister, J. L., et al. (2016). Changes in ocean heat, carbon content, and ventilation: A review of the first decade of GO-SHIP global repeat hydrography. *Annual Review of Marine Science*, 8(1), 185–215. <https://doi.org/10.1146/annurev-marine-052915-100829>
- Tsujino, H., Urakawa, L. S., Griffies, S. M., Danabasoglu, G., Adcroft, A. J., Amaral, A. E., et al. (2020). Evaluation of global ocean–sea-ice model simulations based on the experimental protocols of the Ocean Model Intercomparison Project phase 2 (OMIP-2). *Geoscientific Model Development*, 13(8), 3643–3708. <https://doi.org/10.5194/gmd-13-3643-2020>
- Tsujino, H., Urakawa, S., Nakano, H., Small, R. J., Kim, W. M., Yeager, S. G., et al. (2018). JRA-55 based surface dataset for driving ocean–sea-ice models (JRA55-do). *Ocean Modelling*, 130, 79–139. <https://doi.org/10.1016/j.ocemod.2018.07.002>
- Weijer, W., Cheng, W., Garuba, O. A., Hu, A., & Nadiga, B. T. (2020). CMIP6 models predict significant 21st century decline of the Atlantic Meridional Overturning Circulation. *Geophysical Research Letters*, 47(12). <https://doi.org/10.1029/2019GL086075>
- Worthington, E. L., Moat, B. I., Smeed, D. A., Mecking, J. V., Marsh, R., & McCarthy, G. D. (2021). A 30-year reconstruction of the Atlantic meridional overturning circulation shows no decline. *Ocean Science*, 17(1), 285–299. <https://doi.org/10.5194/os-17-285-2021>
- Wunsch, C. (1996). *The ocean circulation inverse problem*. Cambridge University Press.
- Wunsch, C., & Heimbach, P. (2006). Estimated decadal changes in the North Atlantic meridional overturning circulation and heat flux 1993–2004. *Journal of Physical Oceanography*, 36(11), 2012–2024. <https://doi.org/10.1175/JPO2957.1>

## References From the Supporting Information

- Artana, C., Ferrari, R., Koenig, Z., Sennéchaël, N., Saraceno, M., Piola, A. R., & Provost, C. (2018). Malvinas current volume transport at 41°S: A 24 yearlong time series consistent with mooring data from 3 decades and satellite altimetry. *Journal of Geophysical Research: Oceans*, 123(1), 378–398. <https://doi.org/10.1002/2017JC013600>
- Curry, B., Lee, C. M., Petrie, B., Moritz, R. E., & Kwok, R. (2014). Multiyear volume, liquid freshwater, and sea ice transports through Davis Strait, 2004–10. *Journal of Physical Oceanography*, 44(4), 1244–1266. <https://doi.org/10.1175/jpo-d-13-01177.1>

- Drévilion, M., Bahurel, P., Bazin, D., Benkiran, M., Beuvier, J., Crosnier, L., et al. (2018). Learning about Copernicus Marine Environment Monitoring Service “CMEMS”: A practical introduction to the use of the European Operational Oceanography service. In E. Chassignet, A. Pascual, J. Tintoré, & J. Verron (Eds.), *New frontiers in operational oceanography* (pp. 695–712). GODAE OceanView. <https://doi.org/10.17125/gov2018.ch25>
- Finucane, G., & Hautala, S. (2022). Transport of Antarctic Bottom Water entering the Brazil Basin in a planetary geostrophic inverse model. *Geophysical Research Letters*, *49*(22), 1–9. <https://doi.org/10.1029/2022GL100121>
- Forget, G., Campin, J.-M., Heimbach, P., Hill, C. N., Ponte, R. M., & Wunsch, C. (2015). ECCO version 4: An integrated framework for non-linear inverse modeling and global ocean state estimation. *Geoscientific Model Development*, *8*(10), 3071–3104. <https://doi.org/10.5194/gmd-8-3071-2015>
- Fukumori, I., Wang, O., Fenty, I., Forget, G., Heimbach, P., & Ponte, R. M. (2017). ECCO version 4 release 3. Retrieved from <http://hdl.handle.net/1721.1/102062>
- Ganachaud, A. S. (1999). *Large scale oceanic circulation and fluxes of freshwater, heat, nutrients and oxygen*. Massachusetts Institute of Technology and Woods Hole Oceanographic Institution. <https://doi.org/10.1575/1912/4130>
- Ganachaud, A. S. (2003a). Error budget of inverse box models: The North Atlantic. *Journal of Atmospheric and Oceanic Technology*, *20*(11), 1641–1655. [https://doi.org/10.1175/1520-0426\(2003\)020<1641:EBOIBM>2.0.CO;2](https://doi.org/10.1175/1520-0426(2003)020<1641:EBOIBM>2.0.CO;2)
- Ganachaud, A. S. (2003b). Large-scale mass transports, water mass formation, and diffusivities estimated from World Ocean Circulation Experiment (WOCE) hydrographic data. *Journal of Geophysical Research*, *108*(C7), 3213. <https://doi.org/10.1029/2002jc001565>
- Hogg, N. G., & Owens, W. B. (1999). Direct measurement of the deep circulation within the Brazil Basin. *Deep Sea Research Part II: Topical Studies in Oceanography*, *46*(1–2), 335–353. [https://doi.org/10.1016/S0967-0645\(98\)00097-6](https://doi.org/10.1016/S0967-0645(98)00097-6)
- Hogg, N., Biscaye, P., Gardner, W., & Schmitz, W. J. (1982). On the transport and modification of Antarctic Bottom Water in the Vema Channel. *Journal of Marine Research*, *40*(Supplement), 231–263.
- Holliday, N. P., Bacon, S., Cunningham, S. A., Gary, S. F., Karstensen, J., King, B. A., et al. (2018). Subpolar North Atlantic overturning and gyre-scale circulation in the summers of 2014 and 2016. *Journal of Geophysical Research: Oceans*, *123*(7), 4538–4559. <https://doi.org/10.1029/2018JC013841>
- Lellouche, J.-M., Greiner, E., le Galloudec, O., Garric, G., Regnier, C., Drevillon, M., et al. (2018). Recent updates to the Copernicus Marine Service global ocean monitoring and forecasting real-time 1/12° high-resolution system. *Ocean Science*, *14*(5), 1093–1126. <https://doi.org/10.5194/os-14-1093-2018>
- Lozier, M. S., Li, F., Bacon, S., Bahr, F., Bower, A. S., Cunningham, S. A., et al. (2019). A sea change in our view of overturning in the subpolar North Atlantic. *Science*, *363*(6426), 516–521. <https://doi.org/10.1126/science.aau6592>
- McDonagh, E. L., Bryden, H. L., King, B. A., & Sanders, R. J. (2008). The circulation of the Indian Ocean at 32°S. *Progress in Oceanography*, *79*(1), 20–36. <https://doi.org/10.1016/j.pocean.2008.07.001>
- McDonagh, E. L., McLeod, P., King, B. A., Bryden, H. L., & Valdés, S. T. (2010). Circulation, heat, and freshwater transport at 36°N in the Atlantic. *Journal of Physical Oceanography*, *40*(12), 2661–2678. <https://doi.org/10.1175/2010JPO4176.1>
- Robbins, P. E., & Toole, J. M. (1997). The dissolved silica budget as a constraint on the meridional overturning circulation of the Indian Ocean. *Deep Sea Research Part I: Oceanographic Research Papers*, *44*(5), 879–906. [https://doi.org/10.1016/S0967-0637\(96\)00126-4](https://doi.org/10.1016/S0967-0637(96)00126-4)
- Speer, K. G., Holfort, J., Reynaud, T., & Siedler, G. (1996). South Atlantic heat transport at 11°S. In *The South Atlantic: Present and past circulation* (pp. 105–120).
- Warren, B. A., & Speer, K. G. (1991). Deep circulation in the eastern South Atlantic Ocean. *Deep Sea Research Part A. Oceanographic Research Papers*, *38*(Supplement I), S281–S322. [https://doi.org/10.1016/s0198-0149\(12\)80014-8](https://doi.org/10.1016/s0198-0149(12)80014-8)

**Mass, Heat and Freshwater Transport from Transoceanic Sections in the Atlantic Ocean at 30°S and 24.5°N: Single Sections vs Box Models?**

Verónica Caínzos<sup>1</sup>, Alonso Hernández-Guerra<sup>1</sup>, Riccardo Farneti<sup>2</sup>, M. Dolores Pérez-Hernández<sup>1</sup>, Lynne D. Talley<sup>3</sup>

<sup>1</sup> Unidad Océano y Clima, Instituto de Oceanografía y Cambio Global, IOCAG, Universidad de Las Palmas de Gran Canaria, ULPGC, Unidad Asociada ULPGC-CSIC, Canary Islands, Spain.

<sup>2</sup> The Abdus Salam International Centre for Theoretical Physics (ICTP), Trieste, Italy

<sup>3</sup> Scripps Institution of Oceanography, University of California San Diego, La Jolla, CA, USA

**Contents of this file**

Texts S1 to S4  
Figures S1 to S5  
Tables S1 to S7

## Text S1. Description single-section inverse model 24.5°N

### CONSERVATION EQUATIONS

The inverse model described here is adapted from Hernández-Guerra et al. (2014). The inverse box model for a single section takes the following matrix form:

$$\begin{pmatrix} e_{A_{t,1}} & \cdots & e_{A_{t,n}} & 1 \\ e_{A_{reg}} & \cdots & e_{A_{reg}} & 0 \end{pmatrix} \begin{pmatrix} b_{A_1} \\ \vdots \\ b_{A_n} \\ \Delta T_{AEK} \end{pmatrix} = \begin{pmatrix} y_{A_t} + T_{AEK} \\ y_{A_{reg}} \end{pmatrix},$$

where  $n$  is the number of station pairs for section A,  $q$  is the number of layers,  $b$  are the reference velocities for each station pair,  $\Delta T_{EK}$  is the Ekman transport correction,  $e$  is mass and  $y$  refers to mass transport.

The first equation included is the total conservation for the whole section (denoted with subindex  $t$ ). This equation applies to all station pairs and considers the Ekman correction in the first layer. The following equations are the regional constraints as described below, with different station pairs and neutral density layers affected.

### REFERENCE LEVEL AND VELOCITIES

The reference level of section A05 (24.5°N) is situated in the interphase between NADW and AABW, at  $28.15 \text{ kg m}^{-3}$  for the 1992, 1998, 2004 and 2010 cruises and at  $28.04 \text{ kg m}^{-3}$  for the 2011, 2015-16 and 2020 cruises (Yao Fu et al., 2018; Hernández-Guerra et al., 2014).

### A PRIORI ESTIMATES AND UNCERTAINTIES

The Gauss-Markov method solves this system of equations with a minimum error variance solution from the initial estimates of the unknowns (the velocities at the reference level,  $b$ , and the corrections to the Ekman transport,  $\Delta T_{EK}$ ; Wunsch, 1996). To solve it, we first need a priori estimates and uncertainties that give an initial approximation to the actual value. The preliminary variance of the adjusted velocity at the reference level is  $8 \text{ cm}^2 \text{ s}^{-2}$  for the station pairs closer to coast, where shear is stronger and  $4 \text{ cm}^2 \text{ s}^{-2}$  in the deepest stations. The initial estimates for the mass transport are  $0.36 \text{ Sv}^2$  (the square of the uncertainty of the Bering Strait transport,  $-0.8 \pm 0.6 \text{ Sv}$ ) for the net mass transport across the sections.

The regional constraints applied to each inverse model at 24.5°N are specified in the table below:

Mass constraints	Long	Stations	Layers	Constraint value (Sv)	Adjusted value (Sv)
<b>Florida Strait Current</b>					
1992	Coast-79.2°W	1:10	1:6	$29.2 \pm 2.5$	$29.3 \pm 0.1$
1998	Coast-79.2°W	1:8	1:6	$34.2 \pm 2.3$	$34.2 \pm 0.2$
2004	Coast-79.2°W	1:8	1:6	$31.9 \pm 3.0$	$31.9 \pm 0.3$
2010	Coast-79.2°W	1:11	1:6	$28.5 \pm 3.0$	$28.3 \pm 0.1$
2011	Coast-79.2°W	1:13	1:6	$28.7 \pm 3.0$	$28.7 \pm 0.1$
2015-16	Coast-79.2°W	1:13	1:6	$31.3 \pm 2.5$	$31.3 \pm 0.2$
2020	Coast-79.2°W	1:11	1:6	$33.1 \pm 2.0$	$33.1 \pm 0.2$
<b>Antilles Current</b>					

1992	75.5-72.6°W	11:16	1:6	6.0 ± 8.1	21.6 ± 2.2
1998	76.9-76.2°W	9:18	1:6	6.0 ± 8.1	-15.9 ± 4.1
2004	76.9-76.3°W	9:17	1:6	6.0 ± 8.1	14.7 ± 3.8
2010	76.9-76.1°W	12:23	1:6	6.0 ± 8.1	14.9 ± 0.7
2011	77.1-75.6°W	14:32	1:6	6.0 ± 8.1	20.3 ± 0.9
2015-16	76.9-76.4°W	14:22	1:6	6.0 ± 8.1	5.1 ± 0.5
2020	76.9-76.3°W	12:22	1:6	6.0 ± 8.1	4.7 ± 0.5
<b>DWBC</b>					
1992	75.5-68.0°W	11:23	6:9	-26.5 ± 13.6	-28.2 ± 7.9
1998	76.7-75.1°W	13:24	6:9	-26.5 ± 13.6	15.8 ± 0.6
2004	76.9-75.3°W	9:23	6:9	-26.5 ± 13.6	-13.7 ± 3.8
2010	75.3-71.7°W	27:38	7:9	-26.5 ± 13.6	-15.4 ± 5.1
2011	77.1-71.5°W	14:44	6:9	-26.5 ± 13.6	-15.3 ± 5.1
2015-16	76.9-75.5°W	14:21	6:9	-26.5 ± 13.6	-6.4 ± 1.4
2020	76.9-76.8°W	12:17	6:8	-26.5 ± 13.6	-1.8 ± 0.5

## Text S2. Description single-section inverse model 30°S

### CONSERVATION EQUATIONS

The results from the inverse box modes at 30°S have been obtained from Hernández-Guerra et al. (2019). The matrix form of the inverse model has the form:

$$\begin{pmatrix} e_{A_{t,1}} & \cdots & e_{A_{t,n}} & 1 \\ e_{A_{reg}} & \cdots & e_{A_{reg}} & 0 \end{pmatrix} \begin{pmatrix} b_{A_1} \\ \vdots \\ b_{A_n} \\ \Delta T_{A_{Ek}} \end{pmatrix} = \begin{pmatrix} y_{A_t} + T_{A_{Ek}} \\ y_{A_{reg}} \end{pmatrix},$$

where  $n$  is the number of station pairs for section A,  $q$  is the number of layers,  $b$  are the reference velocities for each station pair,  $\Delta T_{Ek}$  is the Ekman transport correction,  $e$  is mass and  $y$  refers to mass transport.

The first equation included is the total conservation for the whole section (denoted with subindex  $t$ ). This equation applies to all station pairs of and considers the Ekman correction in the first layer. The following equations are the regional constraints as described below, with different station pairs and neutral density layers affected.

### REFERENCE LEVEL AND VELOCITIES

The choice for reference level is at the interphase between the southward flowing North Atlantic Deep Waters (NADW) and the northward flowing Antarctic Bottom Waters (AABW), which lies in the neutral density surface of  $28.15 \text{ kg m}^{-3}$  (Hernández-Guerra et al., 2019; McDonagh et al., 2015).

### A PRIORI ESTIMATES AND UNCERTAINTIES

The Gauss-Markov method solves this system of equations with a minimum error variance solution from the initial estimates of the unknowns (the velocities at the reference level,  $b$ , and the corrections to the Ekman transport,  $\Delta T_{EK}$ ; Wunsch, 1996). To solve it, we first need a priori estimates and uncertainties that give an initial approximation to the actual value. The preliminary variance of the adjusted velocity at the reference level is  $8 \text{ cm}^2 \text{ s}^{-2}$  for the station pairs closer to coast, where shear is stronger and  $4 \text{ cm}^2 \text{ s}^{-2}$  in the deepest stations. The initial estimates for the mass transport are  $0.36 \text{ Sv}^2$  (the square of the uncertainty of the Bering Strait transport,  $-0.8 \pm 0.6 \text{ Sv}$ ) for the net mass transport across the sections.

The regional constraints applied to each inverse model at  $30^\circ\text{S}$  are described in the table below. Note that the constraint imposed for the Brazil Basin is the value used historically, although it has been recently reported that may be overestimated (Finucane & Hautala, 2022).

Mass constraints	Long	Stations	Layers	Constraint value (Sv)	Adjusted value (Sv)
<b>Vema Channel</b>					
1992-93	39.5-38.5°W	21:24	9:11	$4.0 \pm 0.4$	$3.8 \pm 0.4$
2003	40.0-38.0°W	20:25	9:11	$4.0 \pm 0.4$	$3.8 \pm 0.4$
2011	39.8-38.0°W	22:27	9:11	$4.0 \pm 0.4$	$4.0 \pm 0.4$
<b>Brazil Basin</b>					
1992-93	44.8-17.0°W	12:61	9:11	$6.9 \pm 1.8$	$6.4 \pm 2.1$
2003	44.8-15.7°W	12:63	9:11	$6.9 \pm 1.8$	$6.4 \pm 2.0$
2011	45.4-16.0°W	10:64	9:11	$6.9 \pm 1.8$	$6.6 \pm 2.4$
<b>Walvis Ridge N</b>					
1992-93	9.0°W-1.1°E	73:86	9:11	$0 \pm 1$	$-0.3 \pm 1.0$
2003	7.3°W-1.1°E	75:86	9:11	$0 \pm 1$	$-0.3 \pm 1.0$
2011	7.4°W-1.1°E	76:91	9:11	$0 \pm 1$	$-0.2 \pm 0.9$
<b>Walvis Ridge S</b>					
1992-93	2.8-12.2°E	89:101	9:11	$0 \pm 1$	$-0.2 \pm 1.1$
2003	2.3-13.1°E	88:105	9:11	$0 \pm 1$	$-0.1 \pm 1.2$
2011	2.0-13.1°E	93:115	9:11	$0 \pm 1$	$0.0 \pm 1.2$
<b>Brazil Current</b>					
2003	Coast-45.4°W	1:11	1:7	$-40.8 \pm 5.0$	$-38.9 \pm 2.1$
2011	Coast-46.5°W	1:7	1:5	$-12.7 \pm 5.0$	$-10.4 \pm 0.8$
<b>Benguela Current</b>					
2003	11.8°E-Coast	101:110	1:7	$27.4 \pm 5.0$	$26.3 \pm 2.4$
2011	11.3°E-Coast	112:119	1:7	$22.7 \pm 5.0$	$22.6 \pm 2.5$

### Text S3. Description multiple-section inverse models

## CONSERVATION EQUATIONS

The inverse model for each decade links boxes between contiguous sections, from South to North. For each single box, the matrix form of the inverse model equation has the following form:

$$\begin{pmatrix}
 e_{A_t,1} & \cdots & e_{A_t,n} & e_{B_t,1} & \cdots & e_{B_t,m} & 1 & 1 \\
 e_{A_{reg}} & \cdots & e_{A_{reg}} & 0 & \cdots & 0 & 0 & 0 \\
 0 & \cdots & 0 & e_{B_{reg}} & \cdots & e_{B_{reg}} & 0 & 0 \\
 e_{A_{1,1}} & \cdots & e_{A_{1,n}} & e_{B_{1,1}} & \cdots & e_{B_{1,n}} & 1 & 1 \\
 e_{A_{2,1}} & \cdots & e_{A_{2,n}} & e_{B_{2,1}} & \cdots & e_{B_{2,n}} & 0 & 0 \\
 \vdots & \ddots & \vdots & \vdots & \ddots & \vdots & 0 & 0 \\
 \vdots & \ddots & \vdots & \vdots & \ddots & \vdots & \vdots & \vdots \\
 e_{A_{q-1,1}} & \cdots & e_{A_{q-1,n}} & e_{B_{q-1,1}} & \cdots & e_{B_{q-1,n}} & 0 & 0 \\
 e_{A_{q,1}} & \cdots & e_{A_{q,n}} & e_{B_{q,1}} & \cdots & e_{B_{q,n}} & 0 & 0 \\
 s_{A_t,1} & \cdots & s_{A_t,n} & 0 & \cdots & 0 & \left(\frac{s_{A_1}}{e_{A_1}}\right) & 0 \\
 0 & \cdots & 0 & s_{B_t,1} & \cdots & s_{B_t,m} & 0 & \left(\frac{s_{B_1}}{e_{B_1}}\right)
 \end{pmatrix}
 \begin{pmatrix}
 b_{A_1} \\
 \vdots \\
 b_{A_n} \\
 b_{B_1} \\
 \vdots \\
 b_{B_m} \\
 \Delta T_{AEk} \\
 \Delta T_{BEk}
 \end{pmatrix}
 =
 \begin{pmatrix}
 y_{A_t} + y_{B_t} + T_{AEk} + T_{BEk} \\
 y_{A_{reg}} \\
 y_{B_{reg}} \\
 y_{A_1} + y_{B_1} + T_{AEk} + T_{BEk} \\
 y_{A_2} + y_{B_2} \\
 \vdots \\
 \vdots \\
 y_{A_{q-1}} + y_{B_{q-1}} \\
 y_{A_q} + y_{B_q} \\
 z_t + T_{AEk} \cdot \left(\frac{s_{A_1}}{e_{A_1}}\right) \\
 z_{B_t} + T_{BEk} \cdot \left(\frac{s_{B_1}}{e_{B_1}}\right)
 \end{pmatrix},$$

where  $n$  is the number of station pairs for section A,  $m$  is the number of station pairs for section B,  $q$  is the number of layers,  $b$  are the reference velocities for each station pair,  $\Delta T_{EK}$  is the Ekman transport correction,  $e$  is mass,  $s$  is salt,  $y$  is mass transport and  $z$  is the salt transport.

The first equation included in each box is the total conservation for the whole box (denoted with a  $t$  for total). This equation applies to all station pairs of A and B and consider both Ekman corrections in the first layer. The following equations are the regional constraints applied to section A, with different station pairs and neutral density layers affected (Supporting Information Table S7). Similarly, regional equations for section B are found in subsequent files. The following 11 ( $q$  layers) equations correspond to the conservation of each layer between both sections with Ekman correction in the outcropping layers.

In addition to mass conservation, we have also constrained the salinity content of each single section A and B (last two equations). Using salinity instead of mass allows for changes in freshwater across the section while still conserving mass. The salinity transport constrained is 26.0 Sv, resulting from a Bering Strait mass transport of 0.8 Sv with an average salinity of 32.5. For mass conservation, the Ekman parameter used was 1. For salinity conservation, this parameter is expressed as the average ratio between salt and mass at the outcropping layer.

No other properties are conserved in these models. Heat and salt are largely dependent on mass and do not increase the rank of the matrix, therefore failing to add information to the system. The use of property anomalies increases the noise in the system solutions and does not provide a better solution to the inverse model. Top-to-bottom silica conservation has been applied in inverse models when the solution presented large imbalances on the silica budget as in the Indian Ocean (Robbins & Toole, 1997). In the Atlantic Ocean, and specifically in these inverse models, the models already provide solution that satisfy the conservation of silica within each box. Therefore, we do not include these extra equations in the matrix as it would not increase the rank of the matrix or reduce the size of the uncertainties. The solutions come from a highly undetermined system of equations. The system unknowns include the velocities at the reference level and the adjustment to the Ekman transport in the first layer. The Gauss-Markov estimator is applied to solve these matrices (Wunsch, 1996).



## REFERENCE LEVEL AND VELOCITIES

In the South Atlantic, the general choice for reference level is the interphase between the southward flowing North Atlantic Deep Waters (NADW) and the northward flowing Antarctic Bottom Waters (AABW), which lies in the neutral density surface of  $28.15 \text{ kg m}^{-3}$  (Hernández-Guerra et al., 2019; E. L. McDonagh et al., 2015). Section A08 ( $11^\circ\text{S}$ ) in the decade of 1990-99 has basin-specific reference levels between  $27.58$  and  $28.10 \text{ kg m}^{-3}$  (Speer et al., 1996). In the North Atlantic subtropical gyre, the reference level of section A05 ( $24.5^\circ\text{N}$ ) is situated in the interphase between NADW and AABW, at  $28.15 \text{ kg m}^{-3}$  for the 1990-99 and 2000-09 decades and at  $28.04 \text{ kg m}^{-3}$  for the last decade (Yao Fu et al., 2018; Hernández-Guerra et al., 2014). Section A02 ( $47^\circ\text{N}$ ) for the 1990-99 decade presents a reference level at  $28.15 \text{ kg m}^{-3}$  at the interphase between NADW and AABW, whereas for the decade of 2010-19 it is at the interphase between the MOC upper and lower limb at  $27.84 \text{ kg m}^{-3}$  (Ganachaud, 1999). At A03 ( $36^\circ\text{N}$ ), the reference level at the interphase between NADW and AABW is at a neutral density of  $28.04 \text{ kg m}^{-3}$  (McDonagh et al., 2010). The northernmost sections at  $55^\circ\text{N}$  (AR07W+AR07E) show better results when choosing the reference level at the interphase between the MOC upper and lower limb, which lies at  $27.84 \text{ kg m}^{-3}$  (Holliday et al., 2018; Lozier et al., 2019).

## A PRIORI ESTIMATES AND UNCERTAINTIES

The Gauss-Markov method solves this system of equations with a minimum error variance solution from the initial estimates of the unknowns (the velocities at the reference level,  $b$ , and the corrections to the Ekman transport,  $\Delta T_{\text{EK}}$ ; Wunsch, 1996). To solve it, we first need a priori estimates and uncertainties that give an initial approximation to the actual value. The preliminary variance of the adjusted velocity at the reference level is  $8 \text{ cm}^2 \text{ s}^{-2}$  for the station pairs closer to coast, where shear is stronger and  $4 \text{ cm}^2 \text{ s}^{-2}$  in the deepest stations. The initial estimates for the mass transport are  $9 \text{ Sv}^2$  for the net mass transport between two sections, therefore allowing for compensation within each box. For layer conservation, the variance is between 13 and  $1 \text{ Sv}^2$ , decreasing towards deeper layers. The salinity uncertainties are computed as the square of the uncertainty of the Bering Strait transport ( $0.6 \text{ Sv}$ ) times the square of the ration between the total salt transport and the mass transport of each section.

Despite obtaining similar results, this study provides smaller uncertainties than other global inverse solutions (Ganachaud, 2003b) and decadal studies (Fu et al., 2020). This was achieved by using a simpler model with only the velocities at the reference level and the Ekman adjustments as unknowns.

Some of the weaknesses of the inverse model are related to the accurate calculation of the geostrophic transport before the inverse model. We have assumed linear bottom topography between the deepest common level of each station to compute the transport of each bottom triangle. There are uncertainties associated to this approximation, in the order of  $1 \text{ Sv}$ , but can increase in areas of boundary currents along sloping topography (Ganachaud, 2003a; McDonagh et al., 2008; Robbins & Toole, 1997).

The Ekman transport can also be an issue when adjusting the geostrophic transport in surface layers. We believe that the geostrophic calculation of each section is balanced by the Ekman transport for the time of the cruise. There is an adjustment for the instantaneous response of this wind forcing on the upper layers. Using the Ekman transport of the time of the cruise we remove the effect of the seasonal or monthly variability in upper layers. In any case, the Ekman transport is adjusted in the inverse model.

## MULTIPLE CONFIGURATIONS FOR EACH INVERSE MODEL

Instead of obtaining three values for the multiple-section inverse models at 24.5°N, we have computed all possible composites using the seven available sections at this latitude. Therefore, we have added to the three solutions published by Caínzos et al. (2022) four more values.

For the first decade, 1990-99, the original inverse model included the 1992 cruise. We have now applied the same model configuration of that decade for the 1998 cruise. For the second decade, we have included the 2010 section, modifying from the original configuration with the 2004 cruise. For the last decade, the original configuration including the cruise carried out in 2011 was also computed with the 2015-16 and 2020 cruises. The table below summarizes the sections used for each inverse model.

Section	Latitude	Year	Cruise ID	Country
A11	30-45°S	1992	74DI19921222	UK
A10	30°S	1992-93	06MT19921227	DE
A09	19°S	1991	06MT19910210	DE
A08	11°S	1994	06MT19940329	DE
A05	24.5°N	1992	29HE19920714	SP
		1998	31RBOACES24N_2	US
A02	40-50°N	1993	06GA19930612	DE
AR07W	55-60°N	1990	18DA90012	CA
AR07E	55-60°N	1991	74AB62	UK
A10	30°S	2003	49NZ20031106	JA
A095	24°S	2009	740H20090307	UK
A05	24.5°N	2004	74DI20040404	UK
		2010	74DI20100106	UK
A03	36°N	2005	74AB20050501	UK
AR07W	55-60°N	2005	18HU20050526	CA
AR07E	55-60°N	2007	64PE20070830	NE
A10	30°S	2011	33RO20110926	US
A095	19°S	2018	740H20180228	UK
A05	24.5°N	2011	29AH20110128	SP
		2015-16	74EQ20151206	UK
		2020	740H20200119	UK
A02	40-50°N	2013	06M220130509	DE
AR07W	55-60°N	2014	74JC20140606	UK
AR07E	55-60°N	2014	74JC20140606	UK

The 1990-99 inverse model has 112 equations with 643 unknowns for the 1992 cruise and 663 for the 1998 cruise; the 2000-09 model has 83 equations with 506 unknowns for the 2004 cruise and 515 for the 2010 cruise; and the 2010-19 inverse model has 82 equations with 584 unknowns for the 2011 cruise, 551 for the 2015-16 cruise and 547 for the 2020 cruise. The difference in the number of unknowns arise from the different number of pair of stations for each cruise, each associated to an unknown velocity at the reference level.

The only regional constraints affected by the change in the 24.5°N cruise are the values of the Florida Strait transport, which presents small variations, mainly included within their uncertainties:  $31.8 \pm 3.5$ ,  $34.2 \pm 3.0$ ,  $31.9 \pm 3.3$ ,  $28.5 \pm 3.3$ ,  $31.3 \pm 3.4$ ,  $31.3 \pm 3.4$  and  $33.1 \pm 3.4$  Sv for the 1992, 1998, 2004, 2010, 2011, 2015-16 and 2020 cruises, respectively.

#### **Text S4. Additional use of OGCMs**

To complement the use of OGCMs in our study, we have employed two additional numerical models.

ECCOv4r4 (Estimating the Circulation and Climate of the Ocean Version 4 Release 4; ECCO, hereafter) is a data-assimilating model produced by the Jet Propulsion Laboratory. ECCO provides monthly data from 1992 to 2017 with a 1° horizontal resolution (Forget et al., 2015; Fukumori et al., 2017) and 50 vertical levels with varying resolution. ECCOv4r4 assimilates a variety of ocean observations, including satellite altimetry, sea surface temperature (SST) and salinity (SSS), in situ hydrography, ocean mass from satellite gravity and sea-ice concentration. By using its adjoint, ECCO iteratively optimizes surface atmospheric state and internal parameters to fit multiple sources of observations within expected uncertainties, producing a state estimate of the ocean that fits observations and is dynamically consistent.

GLORYS12V1 (GLORYS, hereafter) is a global ocean reanalysis developed by the Copernicus Marine Environment Monitoring Service (CMEMS), released in January 2019, covering the period from 1993 to 2018. The “Nucleus for European Modelling of the Ocean” (NEMO) ocean model is used to generate the reanalysis, driven at the surface by the ECMWF ERA-Interim reanalysis. It assimilates along track altimeter measurements (sea level anomaly), SST, sea ice concentration, and in situ temperature and salinity vertical profiles. Additionally, it employs a 3D-Var scheme to adjust large-scale temperature and salinity biases. The monthly gridded datasets are displayed on a 1/12° grid with 50 standard vertical levels (Drévillon et al., 2018; Lellouche et al., 2018).

Analogously to the analysis performed using GFDL-MOM, we have also computed the anomalies of AMOC, MHT and MFT for ECCO and GLORYS. ECCO anomalies were obtained using mean values of 12.9 Sv, 0.76 PW and -0.041 Sv at 24.5°N and 12.1 Sv, 0.32 PW and 0.128 Sv at 30°S for AMOC, MHT and MFT, respectively. For GLORYS, the anomalies for AMOC, MHT and MFT were computed using mean values of 15.1 Sv, 0.88 PW and 0.229 Sv at 24.5°N and 20.7 Sv, 0.53 PW and 0.097 Sv at 30°S, respectively.

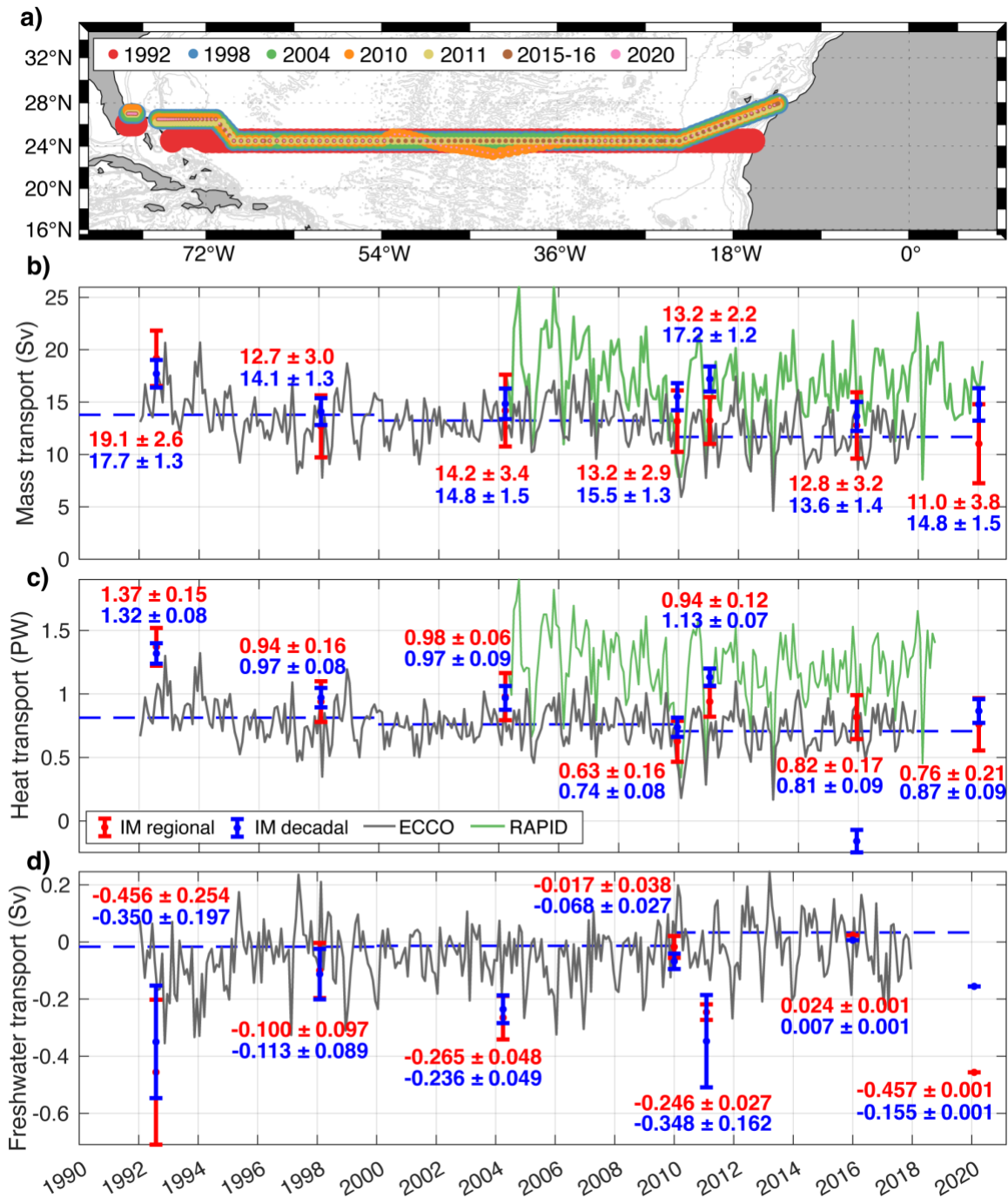


**Figure S1. Estimates at 24.5°N from inverse solutions and RAPID and ECCO time series.** a) Map of the zonal sections included at 24.5°N, with station positions for the A05 cruises in 1992, 1998, 2004, 2010, 2011, 2015-16 and 2020. Monthly time series at 24.5°N (in grey) obtained with ECCO of (b) AMOC anomaly, (c) MHT anomaly and (d) MFT anomaly. Included in subplots (b-d) appear the estimates from the single-section inverse box models in red, and the decadal estimates following Caínzos et al. (2022) in blue. The decadal averages for 1990-99, 2000-09, 2010-19 for each anomaly estimate appear as the blue dashed lines. AMOC and MHT anomaly estimates from the RAPID array time series are shown for comparison in green in subplots (b) and (c), respectively.

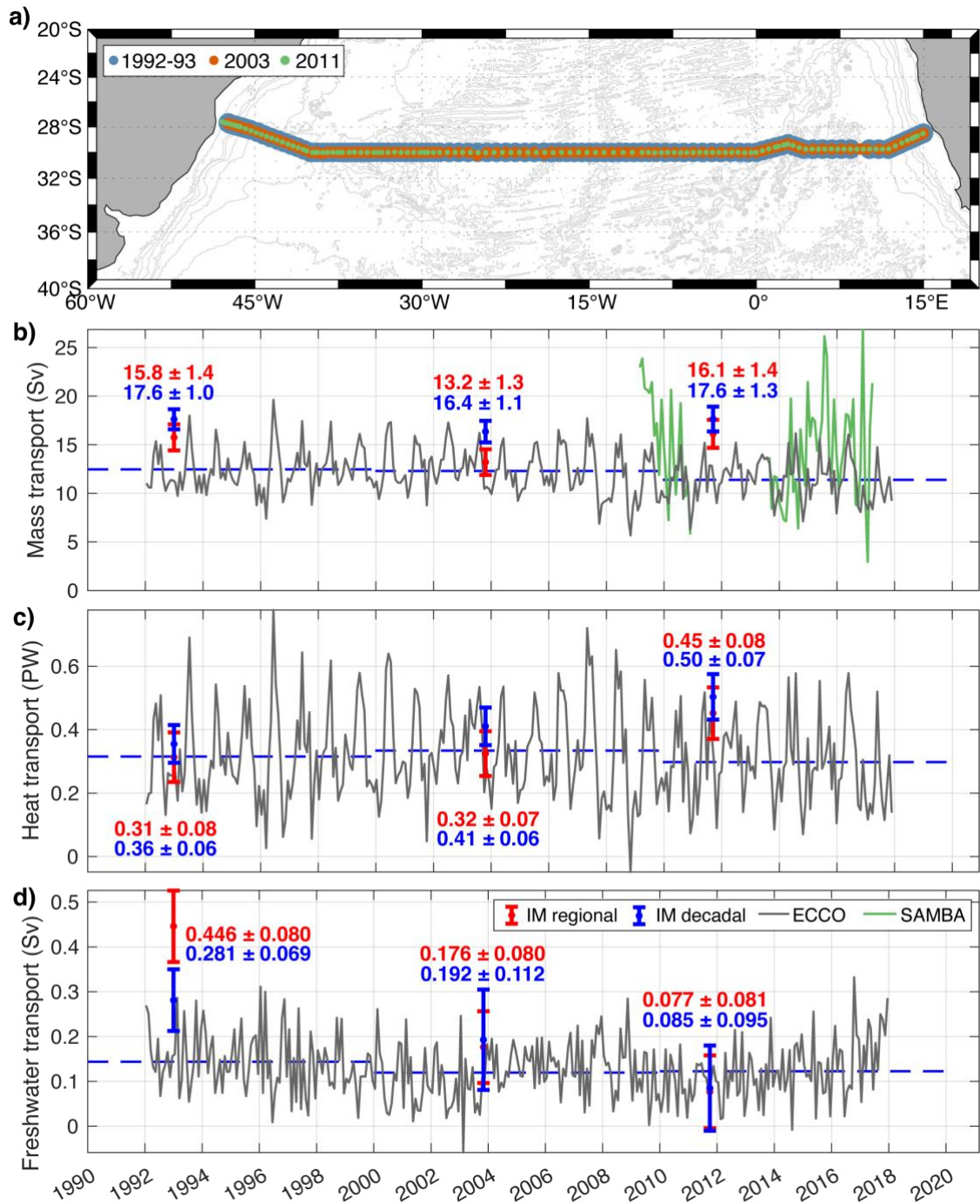


**Figure S2. Estimates at 30°S from inverse solutions and SAMBA and ECCO time series.** a) Map of the zonal sections included at 30°S, with station positions for the A10 cruises in 1992-93, 2003 and 2011. Monthly time series at 30°S (in grey) obtained with ECCO of (b) AMOC anomaly, (c) MHT anomaly and (d) MFT anomaly. Included in subplots (b-d) appear the estimates from the single-section inverse box models from Hernández-Guerra et al. (2019) in red, and the decadal estimates following Caínzos et al. (2022) in blue. The decadal averages for 1990-99, 2000-09, 2010-19 for each anomaly estimate appear as the blue dashed lines. AMOC anomaly estimates from the SAMBA array time series is shown for comparison in green in subplot (b).

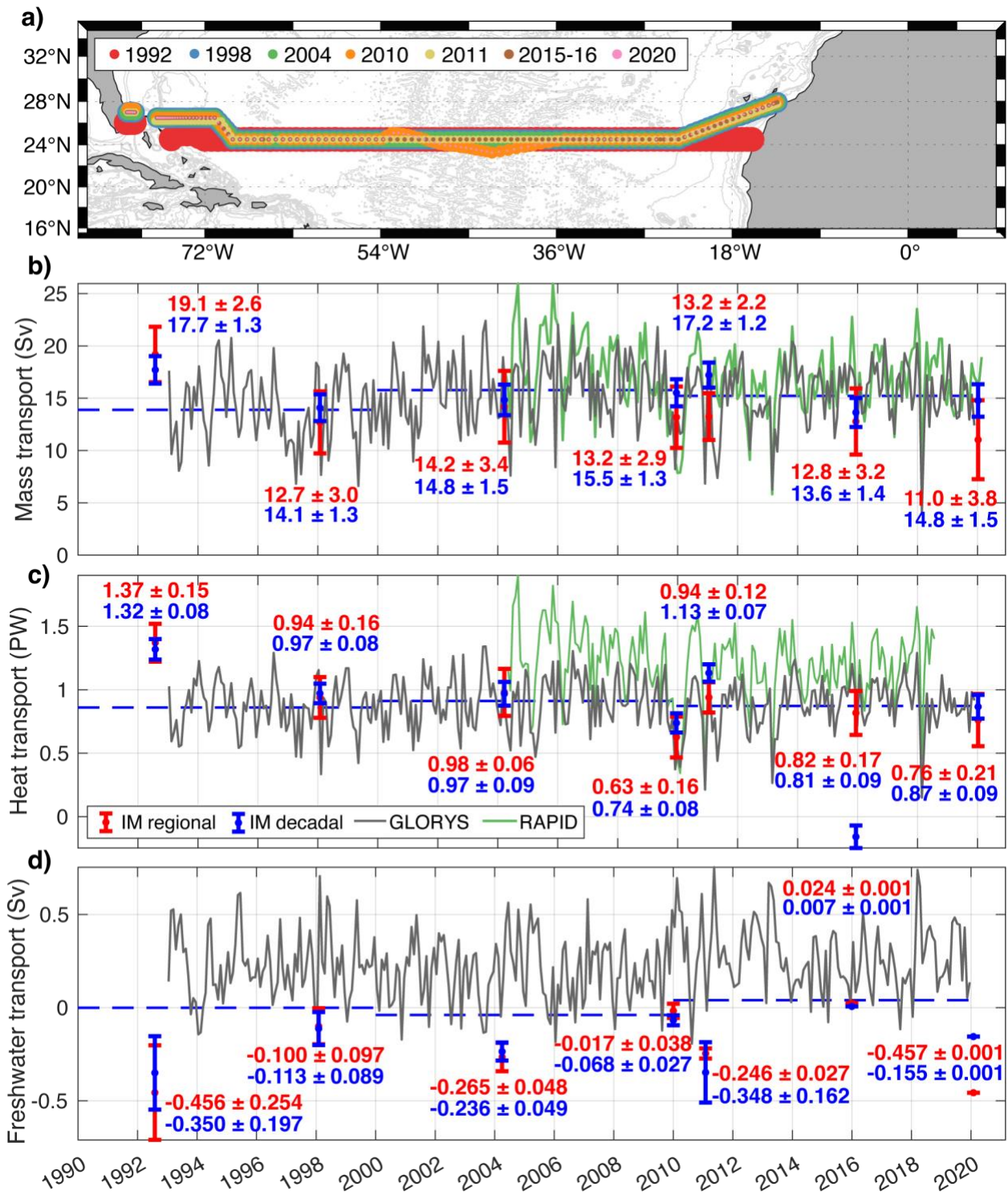


**Figure S3.** Same as Figure S1 but using GLORYS.

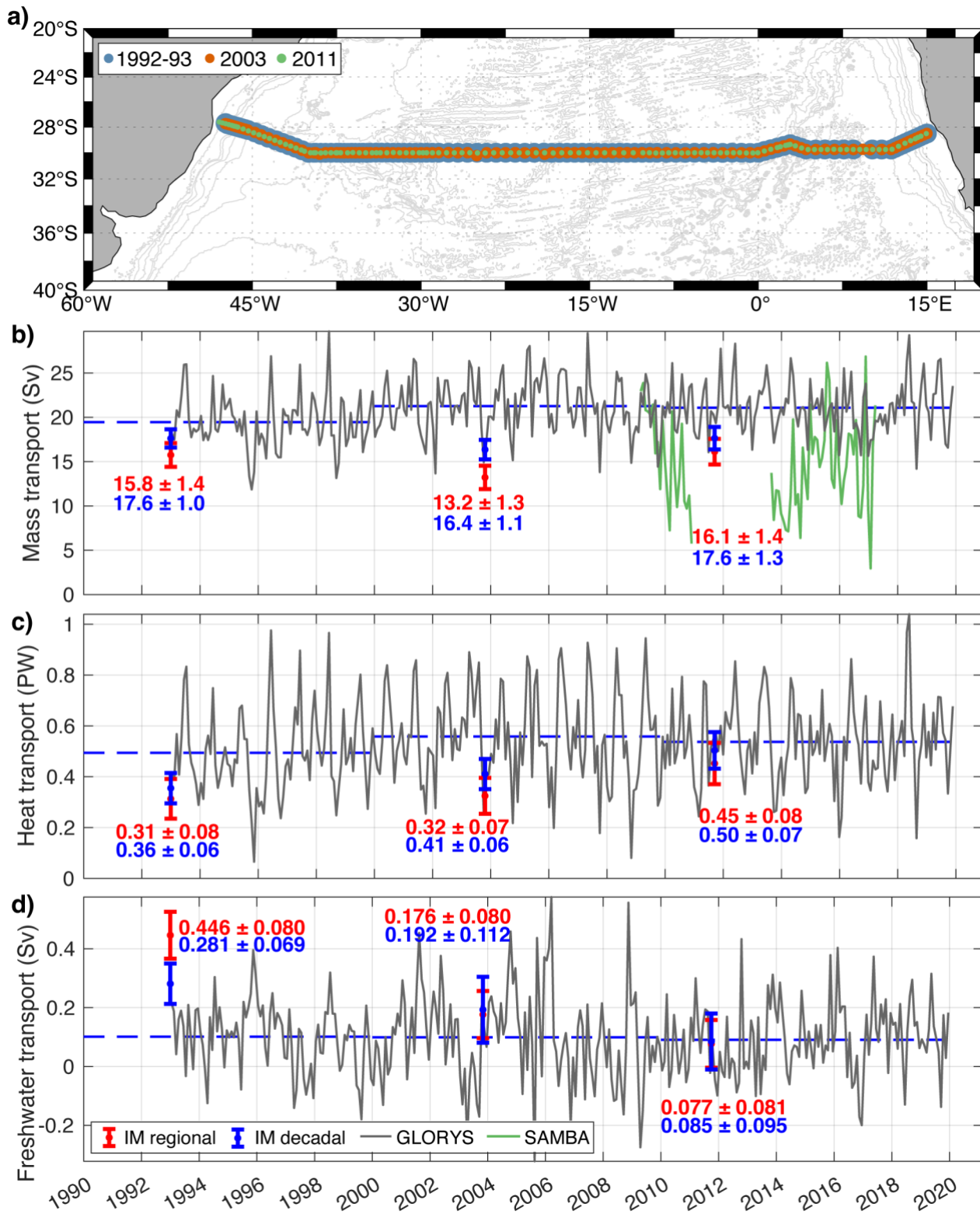


**Figure S4.** Same as Figure S2 but using GLORYS.

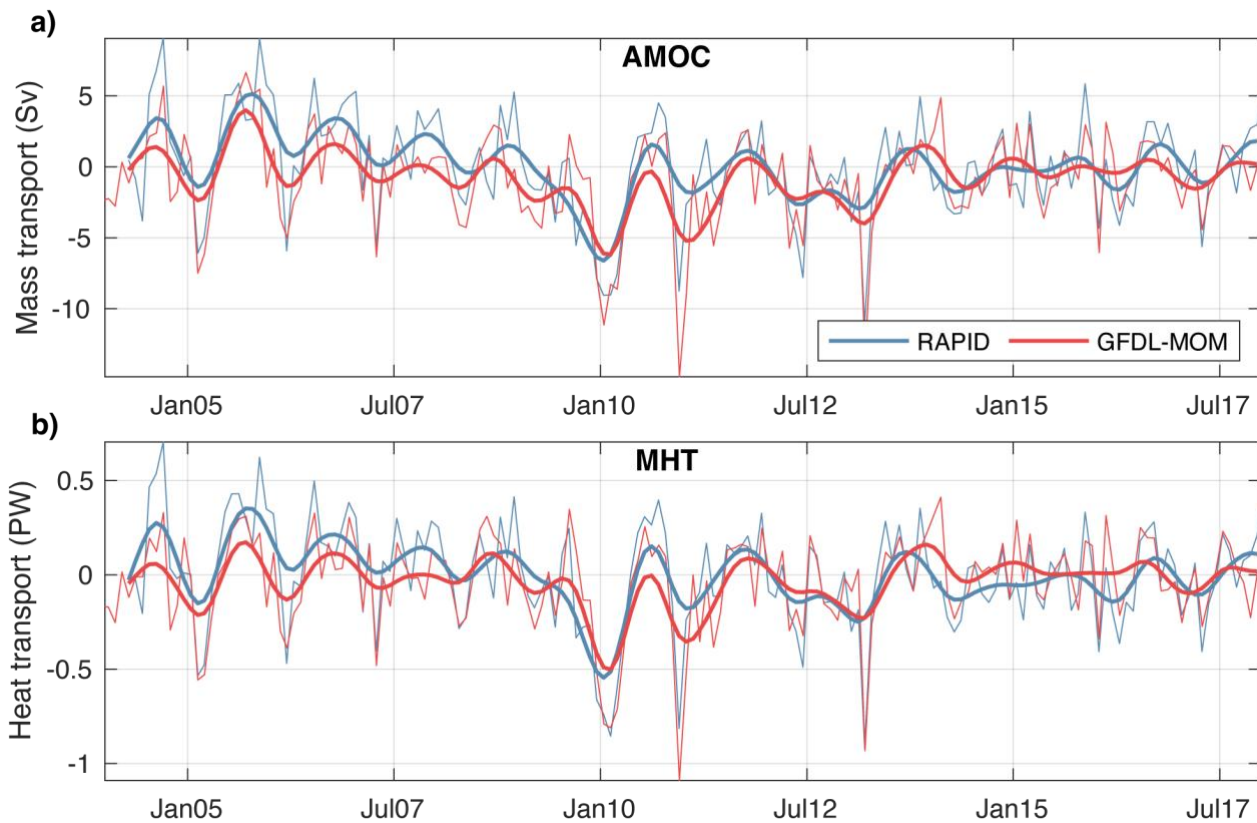


**Figure S5. Agreement on interannual scales for 24.5°N between RAPID and GFDL-MOM for AMOC and MHT.** Time series of RAPID (blue lines) and GFDL-MOM (red lines) for AMOC (a) and MHT (b) anomalies. Bold lines represent the 2<sup>nd</sup> order Butterworth-filtered signals with a 1-year cut-off period to remove any subannual frequencies. Thin lines show the monthly values of each record. The filtered signal for AMOC presents a standard deviation of 2.1 Sv for RAPID and 1.8 Sv for MOM. On the other hand, the filtered signal for MHT shows a standard deviation of 0.15 PW for the RAPID signal and 0.12 PW for GFDL-MOM. For these signals, the correlation coefficient ( $R^2$ ) presents relatively large values, indicating also strong correlation between RAPID and GFDL-MOM (0.7 for MOC and 0.6 for MHT) on interannual timescales.



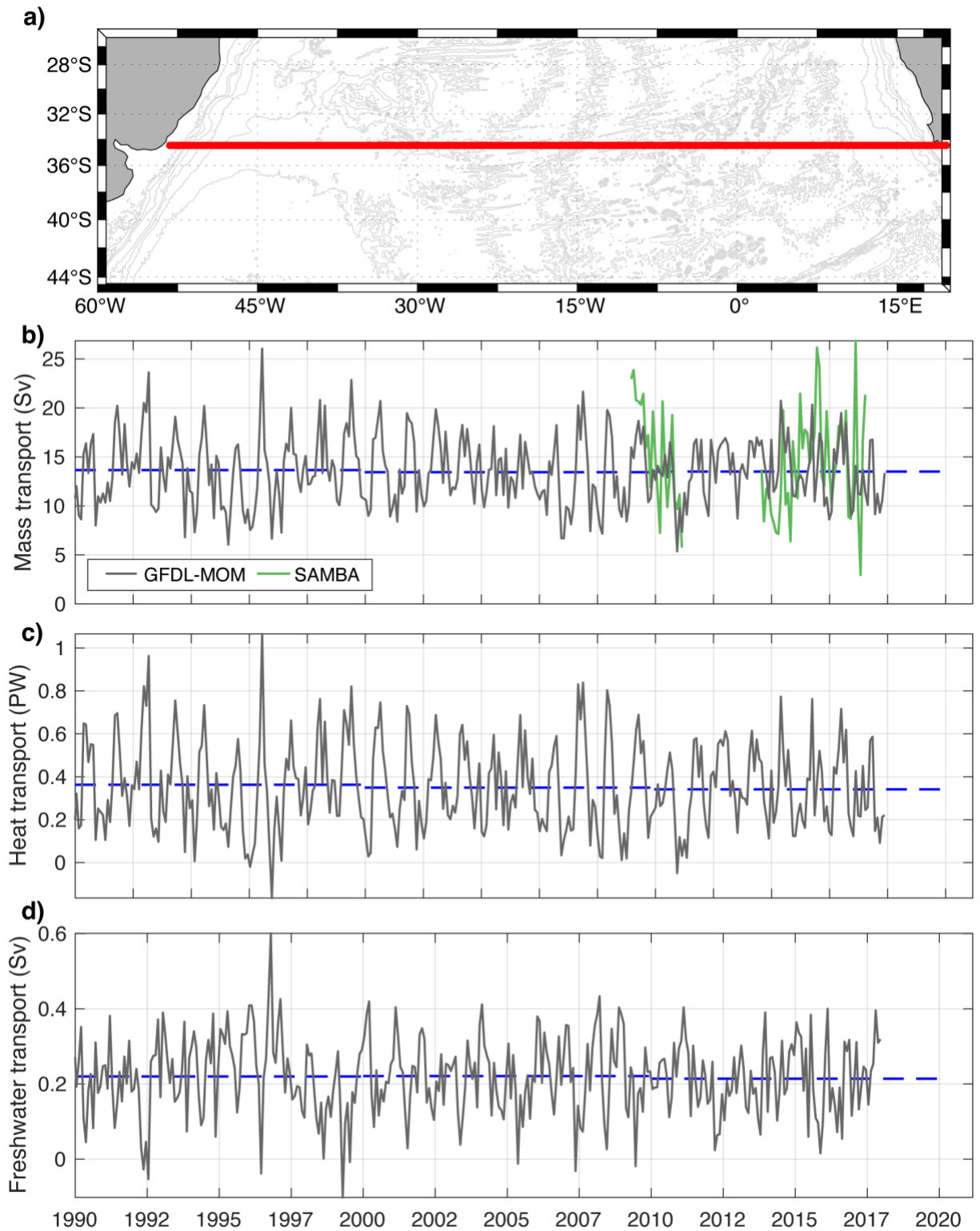


**Figure S6.** Estimates at 34.5°S from SAMBA and GFDL-MOM time series. a) Map of the zonal section included at 34.5°S. Monthly time series at 34.5°S (in grey) obtained with GFDL-MOM of (b) AMOC, (c) MHT and (d) MFT. AMOC estimates from the SAMBA array time series is shown for comparison in green in subplot (b).

**Table S1. Zonal sections used for each latitude.**

<i>Section</i>	<i>Year</i>	<i>Date</i>	<i>Country</i>	<i>Chief Scientist</i>
24.5°N	1992	14 Jul - 15 Aug	Spain	G. Parrilla
	1998	23 Jan - 24 Feb	United States	D. S. Bitterman & K. Lee
	2004	04 Apr - 10 May	United Kingdom	S. Cunningham
	2010	06 Jan - 18 Feb	United Kingdom	B. King
	2011	28 Jan - 14 Mar	Spain	A. Hernández-Guerra
	2015-16	06 Dec - 22 Jan	United Kingdom	B. King
	2020	19 Jan - 01 Mar	United Kingdom	A. Sánchez-Franks
30°S	1992-93	27 Dec - 31 Jan	Germany	T. Müller
	2003	06 Nov - 05 Dec	Japan	Y. Yoshikawa
	2011	26 Sep - 31 Oct	United States	M. Baringer & A. Macdonald

**Table S2. Time of cruise averages at 24.5°N and 30°S for AMOC (in Sv), MHT (in PW) and MFT (in Sv) and their anomalies.** In this table we are comparing the results from the single sections and the GFDL-MOM values for the time of the cruise.

	<i>Cruise</i>	<i>Single section Absolute value</i>	<i>Single section Anomaly</i>	<i>GFDL-MOM Absolute value</i>	<i>GFDL-MOM Anomaly</i>
<b>24.5°N</b>					
AMOC (Sv)	1992	19.1 ± 2.6	5.4 ± 2.9	18.1 ± 1.3	5.1 ± 1.3
	1998	12.7 ± 3.0	-1.1 ± 3.2	10.1 ± 1.4	-2.9 ± 1.4
	2004	14.2 ± 3.4	0.4 ± 3.6	12.7 ± 0.8	-0.4 ± 0.8
	2010	13.2 ± 2.9	-0.6 ± 3.1	8.7 ± 3.6	-4.3 ± 3.6
	2011	13.2 ± 2.2	-0.5 ± 2.5	8.3 ± 4.2	-4.7 ± 4.2
	2015-16	12.8 ± 3.2	-1.0 ± 3.4	10.6 ± 3.6	-2.4 ± 3.6
	2020	11.0 ± 3.8	-2.7 ± 3.9	-	-
MHT (PW)	1992	1.37 ± 0.15	0.45 ± 0.17	1.13 ± 0.09	0.33 ± 0.09
	1998	0.94 ± 0.16	0.02 ± 0.17	0.64 ± 0.09	-0.16 ± 0.09
	2004	0.98 ± 0.19	0.06 ± 0.20	0.73 ± 0.05	-0.06 ± 0.05
	2010	0.63 ± 0.16	-0.29 ± 0.17	0.46 ± 0.20	-0.33 ± 0.20
	2011	0.94 ± 0.12	0.02 ± 0.13	0.54 ± 0.25	-0.25 ± 0.25
	2015-16	0.82 ± 0.17	-0.11 ± 0.18	0.70 ± 0.25	-0.09 ± 0.25
	2020	0.76 ± 0.21	-0.16 ± 0.22	-	-
MFT (Sv)	1992	-0.456 ± 0.254	-0.239 ± 0.257	-0.321 ± 0.103	-0.212 ± 0.103
	1998	-0.100 ± 0.097	0.117 ± 0.105	0.065 ± 0.087	0.174 ± 0.087
	2004	-0.265 ± 0.048	-0.048 ± 0.086	-0.161 ± 0.050	-0.052 ± 0.050
	2010	-0.017 ± 0.038	0.199 ± 0.056	0.171 ± 0.171	0.281 ± 0.171
	2011	-0.246 ± 0.027	-0.029 ± 0.049	0.063 ± 0.295	0.173 ± 0.295
	2015-16	0.024 ± 0.001	0.240 ± 0.041	0.056 ± 0.175	0.166 ± 0.175
	2020	-0.457 ± 0.001	-0.240 ± 0.041	-	-
<b>30°S</b>					
AMOC (Sv)	1992-93	15.8 ± 1.3	0.7 ± 1.4	14.0 ± 1.6	0.4 ± 1.6
	2003	13.2 ± 1.3	-1.8 ± 1.4	12.2 ± 1.2	-1.4 ± 1.2
	2011	16.1 ± 1.4	1.1 ± 1.5	13.6 ± 0.2	0.1 ± 0.2
MHT (PW)	1992-93	0.31 ± 0.08	-0.05 ± 0.08	0.38 ± 0.09	-0.02 ± 0.09
	2003	0.32 ± 0.07	-0.04 ± 0.07	0.27 ± 0.02	-0.12 ± 0.02
	2011	0.45 ± 0.08	0.09 ± 0.08	0.44 ± 0.04	0.05 ± 0.04
MFT (Sv)	1992-93	0.446 ± 0.080	0.213 ± 0.080	0.127 ± 0.056	0.020 ± 0.056
	2003	0.176 ± 0.080	-0.057 ± 0.080	0.192 ± 0.033	0.085 ± 0.033
	2011	0.077 ± 0.081	-0.156 ± 0.081	0.077 ± 0.046	-0.030 ± 0.046

**Table S3. Decadal averages at 24.5°N and 30°S for AMOC (in Sv), MHT (in PW) and MFT (in Sv) and their anomalies.** In this table we are comparing the results from the multiple-section inverse estimates from Caínzos et al. (2022) and the decadal averages from GFDL-MOM.

	Decade	Multiple sections Absolute value	Multiple sections Anomaly	GFDL-MOM Absolute value	GFDL-MOM Anomaly
<b>24.5°N</b>					
<i>AMOC</i> (Sv)	1990-99 (92)	17.7 ± 1.3	2.3 ± 1.4	13.6 ± 0.3	0.6 ± 0.3
	1990-99 (98)	14.1 ± 1.3	-1.3 ± 1.4	13.6 ± 0.3	0.6 ± 0.3
	2000-09 (04)	14.8 ± 1.5	-0.6 ± 1.5	13.1 ± 0.3	0.1 ± 0.3
	2000-09 (10)	15.5 ± 1.3	0.1 ± 1.4	13.1 ± 0.3	0.1 ± 0.3
	2010-19 (11)	17.2 ± 1.2	1.8 ± 1.3	11.8 ± 0.3	-1.2 ± 0.3
	2010-19 (15)	13.6 ± 1.4	-1.8 ± 1.5	11.8 ± 0.3	-1.2 ± 0.3
	2010-19 (20)	14.8 ± 1.5	-0.6 ± 1.6	11.8 ± 0.3	-1.2 ± 0.3
<i>MHT</i> (PW)	1990-99 (92)	1.32 ± 0.08	0.35 ± 0.09	0.82 ± 0.02	0.02 ± 0.02
	1990-99 (98)	0.97 ± 0.08	-0.00 ± 0.08	0.82 ± 0.02	0.02 ± 0.02
	2000-09 (04)	0.97 ± 0.09	-0.00 ± 0.10	0.80 ± 0.02	0.01 ± 0.02
	2000-09 (10)	0.74 ± 0.08	-0.23 ± 0.08	0.80 ± 0.02	0.01 ± 0.02
	2010-19 (11)	1.13 ± 0.07	0.16 ± 0.07	0.74 ± 0.03	-0.06 ± 0.03
	2010-19 (15)	0.81 ± 0.09	-0.16 ± 0.09	0.74 ± 0.03	-0.06 ± 0.03
	2010-19 (20)	0.87 ± 0.09	-0.11 ± 0.10	0.74 ± 0.03	-0.06 ± 0.03
<i>MFT</i> (Sv)	1990-99 (92)	-0.350 ± 0.197	-0.170 ± 0.201	-0.127 ± 0.019	-0.017 ± 0.019
	1990-99 (98)	-0.113 ± 0.089	0.068 ± 0.097	-0.127 ± 0.019	-0.017 ± 0.019
	2000-09 (04)	-0.236 ± 0.049	-0.055 ± 0.063	-0.119 ± 0.015	-0.010 ± 0.015
	2000-09 (10)	-0.068 ± 0.027	0.113 ± 0.048	-0.119 ± 0.015	-0.010 ± 0.015
	2010-19 (11)	-0.348 ± 0.162	-0.167 ± 0.167	-0.057 ± 0.024	0.053 ± 0.024
	2010-19 (15)	0.007 ± 0.001	0.187 ± 0.039	-0.057 ± 0.024	0.053 ± 0.024
	2010-19 (20)	-0.155 ± 0.001	0.025 ± 0.039	-0.057 ± 0.024	0.053 ± 0.024
<b>30°S</b>					
<i>AMOC</i> (Sv)	1990-99	17.6 ± 1.0	0.4 ± 1.1	13.6 ± 0.3	0.0 ± 0.3
	2000-09	16.4 ± 1.1	-0.9 ± 1.1	13.6 ± 0.3	0.1 ± 0.3
	2010-19	17.6 ± 1.3	0.4 ± 1.3	13.6 ± 0.3	0.1 ± 0.3
<i>MHT</i> (PW)	1990-99	0.36 ± 0.06	-0.07 ± 0.06	0.39 ± 0.02	0.00 ± 0.02
	2000-09	0.41 ± 0.06	-0.01 ± 0.06	0.40 ± 0.02	0.01 ± 0.02
	2010-19	0.50 ± 0.07	0.08 ± 0.07	0.38 ± 0.02	-0.01 ± 0.02
<i>MFT</i> (Sv)	1990-99	0.281 ± 0.069	0.095 ± 0.069	0.113 ± 0.009	0.007 ± 0.009
	2000-09	0.193 ± 0.112	0.007 ± 0.112	0.107 ± 0.009	0.001 ± 0.009
	2010-19	0.085 ± 0.095	-0.012 ± 0.095	0.097 ± 0.009	-0.009 ± 0.009

**Table S4. Time of cruise averages at 24.5°N and 30°S for AMOC (in Sv), MHT (in PW) and MFT (in Sv) and their anomalies for the additional OGCMs used for comparison (ECCO and GLORYS).**

	<i>Cruise</i>	<i>ECCO Absolute value</i>	<i>ECCO Anomaly</i>	<i>GLORYS Absolute value</i>	<i>GLORYS Anomaly</i>
<b>24.5°N</b>					
AMOC (Sv)	1992	17.0 ± 0.6	4.1 ± 0.6	-	-
	1998	10.7 ± 2.9	-2.3 ± 2.9	14.1 ± 2.6	-1.0 ± 2.6
	2004	13.1 ± 0.9	0.1 ± 0.9	15.6 ± 1.8	0.5 ± 1.8
	2010	7.2 ± 1.2	-5.7 ± 1.2	11.7 ± 0.1	-3.4 ± 0.1
	2011	10.8 ± 1.6	-2.1 ± 1.6	12.5 ± 2.2	-2.5 ± 2.2
	2015-16	10.1 ± 1.6	-2.8 ± 1.6	12.2 ± 0.1	-2.9 ± 0.1
	2020	-	-	-	-
MHT (PW)	1992	1.01 ± 0.06	0.25 ± 0.06	-	-
	1998	0.60 ± 0.25	-0.16 ± 0.25	0.88 ± 0.19	-0.00 ± 0.19
	2004	0.76 ± 0.06	-0.00 ± 0.06	0.83 ± 0.12	-0.05 ± 0.12
	2010	0.29 ± 0.11	-0.47 ± 0.11	0.47 ± 0.07	-0.42 ± 0.07
	2011	0.57 ± 0.15	-0.19 ± 0.15	0.71 ± 0.13	-0.18 ± 0.13
	2015-16	0.70 ± 0.15	-0.06 ± 0.15	0.71 ± 0.01	-0.17 ± 0.01
	2020	-	-	-	-
MFT (Sv)	1992	-0.183 ± 0.052	-0.093 ± 0.052	-	-
	1998	0.020 ± 0.169	0.109 ± 0.169	0.164 ± 0.181	0.007 ± 0.181
	2004	-0.090 ± 0.046	-0.001 ± 0.046	0.118 ± 0.151	-0.039 ± 0.151
	2010	0.092 ± 0.093	0.181 ± 0.093	0.557 ± 0.093	0.400 ± 0.093
	2011	-0.076 ± 0.049	0.014 ± 0.049	0.238 ± 0.112	0.081 ± 0.112
	2015-16	-0.034 ± 0.080	0.056 ± 0.080	0.292 ± 0.010	0.135 ± 0.010
	2020	-	-	-	-
<b>30°S</b>					
AMOC (Sv)	1992-93	11.2 ± 0.1	-0.8 ± 0.1	20.4 ± 0.4	-0.3 ± 0.4
	2003	10.4 ± 0.2	-1.7 ± 0.2	19.1 ± 1.0	-1.7 ± 1.0
	2011	11.9 ± 0.9	-0.2 ± 0.9	20.4 ± 1.1	-0.3 ± 1.1
MHT (PW)	1992-93	0.26 ± 0.01	-0.06 ± 0.01	0.49 ± 0.08	-0.05 ± 0.08
	2003	0.22 ± 0.04	-0.10 ± 0.04	0.44 ± 0.03	-0.10 ± 0.03
	2011	0.33 ± 0.05	0.01 ± 0.05	0.54 ± 0.04	0.00 ± 0.04
MFT (Sv)	1992-93	0.158 ± 0.002	0.030 ± 0.002	0.110 ± 0.061	0.008 ± 0.061
	2003	0.148 ± 0.024	0.019 ± 0.024	0.147 ± 0.040	0.045 ± 0.040
	2011	0.089 ± 0.014	-0.039 ± 0.014	0.009 ± 0.049	-0.093 ± 0.049

**Table S5. Decadal averages at 24.5°N and 30°S for AMOC (in Sv), MHT (in PW) and MFT (in Sv) and their anomalies for the additional OGCMs used for comparison (ECCO and GLORYS).**

	Decade	ECCO Absolute value	ECCO Anomaly	GLORYS Absolute value	GLORYS Anomaly
<b>24.5°N</b>					
<i>AMOC</i> (Sv)	1990-99 (92)	13.8 ± 0.3	0.9 ± 0.3	13.9 ± 0.4	-1.2 ± 0.4
	1990-99 (98)	13.8 ± 0.3	0.9 ± 0.3	13.9 ± 0.4	-1.2 ± 0.4
	2000-09 (04)	13.2 ± 0.2	0.3 ± 0.2	15.8 ± 0.3	0.7 ± 0.3
	2000-09 (10)	13.2 ± 0.2	0.3 ± 0.2	15.8 ± 0.3	0.7 ± 0.3
	2010-19 (11)	11.7 ± 0.2	-1.2 ± 0.2	15.2 ± 0.3	0.1 ± 0.3
	2010-19 (15)	11.7 ± 0.2	-1.2 ± 0.2	15.2 ± 0.3	0.1 ± 0.3
	2010-19 (20)	11.7 ± 0.2	-1.2 ± 0.2	15.2 ± 0.3	0.1 ± 0.3
<i>MHT</i> (PW)	1990-99 (92)	0.81 ± 0.02	0.05 ± 0.02	0.86 ± 0.02	-0.02 ± 0.02
	1990-99 (98)	0.81 ± 0.02	0.05 ± 0.02	0.86 ± 0.02	-0.02 ± 0.02
	2000-09 (04)	0.76 ± 0.01	0.00 ± 0.01	0.91 ± 0.02	0.03 ± 0.02
	2000-09 (10)	0.76 ± 0.01	0.00 ± 0.01	0.91 ± 0.02	0.03 ± 0.02
	2010-19 (11)	0.71 ± 0.02	-0.05 ± 0.02	0.87 ± 0.02	-0.01 ± 0.02
	2010-19 (15)	0.71 ± 0.02	-0.05 ± 0.02	0.87 ± 0.02	-0.01 ± 0.02
	2010-19 (20)	0.71 ± 0.02	-0.05 ± 0.02	0.87 ± 0.02	-0.01 ± 0.02
<i>MFT</i> (Sv)	1990-99 (92)	-0.107 ± 0.013	-0.017 ± 0.013	0.162 ± 0.021	0.006 ± 0.021
	1990-99 (98)	-0.107 ± 0.013	-0.017 ± 0.013	0.162 ± 0.021	0.006 ± 0.021
	2000-09 (04)	-0.103 ± 0.009	-0.014 ± 0.009	0.116 ± 0.017	-0.041 ± 0.017
	2000-09 (10)	0.103 ± 0.009	-0.014 ± 0.009	0.116 ± 0.017	-0.041 ± 0.017
	2010-19 (11)	-0.055 ± 0.012	0.034 ± 0.012	0.194 ± 0.018	0.037 ± 0.018
	2010-19 (15)	-0.055 ± 0.012	0.034 ± 0.012	0.194 ± 0.018	0.037 ± 0.018
	2010-19 (20)	-0.055 ± 0.012	0.034 ± 0.012	0.194 ± 0.018	0.037 ± 0.018
<b>30°S</b>					
<i>AMOC</i> (Sv)	1990-99	12.5 ± 0.2	0.4 ± 0.2	19.4 ± 0.3	-1.3 ± 0.3
	2000-09	12.3 ± 0.2	0.2 ± 0.2	21.3 ± 0.3	0.5 ± 0.3
	2010-19	11.4 ± 0.2	-0.7 ± 0.2	21.1 ± 0.3	0.4 ± 0.3
<i>MHT</i> (PW)	1990-99	0.32 ± 0.01	-0.00 ± 0.01	0.49 ± 0.02	-0.04 ± 0.02
	2000-09	0.33 ± 0.01	0.02 ± 0.01	0.56 ± 0.02	0.02 ± 0.02
	2010-19	0.30 ± 0.01	-0.02 ± 0.01	0.54 ± 0.01	0.00 ± 0.01
<i>MFT</i> (Sv)	1990-99	0.144 ± 0.007	0.016 ± 0.007	0.115 ± 0.013	0.013 ± 0.013
	2000-09	0.120 ± 0.006	-0.009 ± 0.006	0.104 ± 0.015	0.002 ± 0.015
	2010-19	0.123 ± 0.007	-0.005 ± 0.007	0.090 ± 0.011	-0.011 ± 0.011

**Table S6. Root Mean Squared Errors (RMSE) for 24.5°N and 30°S for the anomalies of AMOC (Sv), MHT (PW) and MFT (Sv)** comparing the values from the single-section inverse models of this study and the multiple-section inverse model solutions as in Caínzos et al. (2022) with ECCO and GLORYS values for both the time of the cruise and the decadal averages. For reference, at 24.5°N, ECCO presents a standard deviation of 2.3 Sv for AMOC, 0.16 PW for MHT and 0.114 Sv for MFT. At 30°S, the standard deviations for AMOC, MHT and MFT are, respectively, 2.3 Sv, 0.14 PW and 0.069 Sv. For GLORYS at 24.5°N, the standard deviations are 3.3 Sv, 0.20 PW and 0.191 Sv for MOC, MHT and MFT. These values at 30°S for MOC, MHT and MFT are 3.1 Sv, 0.17 PW and 0.140 Sv, respectively.

		<i>ECCO</i> <i>cruise</i>	<i>ECCO</i> <i>decadal</i>	<i>GLORYS</i> <i>cruise</i>	<i>GLORYS</i> <i>decadal</i>
<b>24.5°N</b>					
<i>Single-section</i> <i>inverse model</i>	RMSE AMOC (Sv)	<b>2.0</b>	2.4	<b>2.2</b>	3.6
	RMSE MHT (PW)	<b>0.17</b>	0.19	<b>0.18</b>	0.23
	RMSE MFT (Sv)	<b>0.188</b>	0.274	<b>0.213</b>	0.279
<i>Multiple-section</i> <i>inverse model</i>	RMSE AMOC (Sv)	2.7	<b>1.6</b>	2.7	<b>2.0</b>
	RMSE MHT (PW)	0.17	<b>0.14</b>	<b>0.15</b>	0.17
	RMSE MFT (Sv)	<b>0.229</b>	0.259	0.276	<b>0.263</b>
<b>30°S</b>					
<i>Single-section</i> <i>inverse model</i>	RMSE AMOC (Sv)	<b>1.5</b>	1.6	<b>1.4</b>	1.9
	RMSE MHT (PW)	<b>0.03</b>	0.08	<b>0.04</b>	0.07
	RMSE MFT (Sv)	<b>0.175</b>	0.197	<b>0.189</b>	0.217
<i>Multiple-section</i> <i>inverse model</i>	RMSE AMOC (Sv)	3.5	<b>2.8</b>	3.4	<b>3.0</b>
	RMSE MHT (PW)	0.09	<b>0.08</b>	0.09	<b>0.06</b>
	RMSE MFT (Sv)	<b>0.085</b>	0.109	<b>0.099</b>	0.126

**Table S7.** Regional constraints applied to each section for the 1990-99 inverse model. The sixth column represents the imposed value in the model; the seventh column is the mass transport before the model, and the eighth column is the value after the inverse model. The uncertainties for the mass transport adjusted with the inverse model (eighth column) are part of the results of the inverse model using the Gauss-Markov estimator.

Mass constraints	Long	Depth	Stations	Layers	Constraint value (Sv)	Initial transport (Sv)	Adjusted transport (Sv)	References
<b>1990-99 decade</b>								
A11 (1992)								
WBC (Malvinas current)	60-57.8°W	All	1:4	1:11	37.1 ± 6.6	37.1	38.0 ± 2.0	Artana et al. (2018)
Cape Basin AABW	8.2°W-10.9°E	Bottom	58:80	9:11	0 ± 0.5	1.0	0.0 ± 0.9	McDonagh & King (2005)
Argentine Basin AABW	57-15°W	Bottom	9:51	9:11	6 ± 1	-1.5	5.9 ± 1.6	McDonagh & King (2005)
A10 (1992)								
Brazil basin	45-15.3°W	Bottom	12:63	9:11	6.9 ± 1.8	3.0	4.5 ± 1.7	Hogg & Owens (1999)
Vema channel	39.7-37.7°W	AABW	21:25	9:11	4.0 ± 0.4	1.5	3.8 ± 0.4	Hogg et al. (1982)
Walvis R. North	7.3°W-1.7°E	Bottom	75:87	9:11	0 ± 1	-0.2	-0.5 ± 0.9	Warren & Speer (1991)
Walvis R. South	2.2-13.4°E	Bottom	88:106	9:11	0 ± 1	0.7	-0.8 ± 1.3	Warren & Speer (1991)
Brazil current	Coast-44.8°W	Surf - interm	1:12	1:7	-38.9 ± 2.1	-16.3	-38.2 ± 1.3	Hernández-Guerra et al. (2019)
Benguela current	11.8°E-Coast	Surf - interm	101:110	1:7	26.3 ± 2.4	19.7	25.8 ± 1.4	Hernández-Guerra et al. (2019)
A05 + Florida (1992)								
Florida Current	All	All	1:10	1:5	31.8 ± 3.5	31.8	31.8 ± 0.3	Florida Current Project
AR07W (1990)								
Bering Strait (Davis Strait)	All	All	1:21	1:11	-1.6 ± 0.2	1.0	-1.6 ± 1.2	Curry et al. (2014)



AR07E (1993)									
Bering Strait (East)	All	All	22:58	1:11	$0.80 \pm 0.63$	5.7	$0.7 \pm 3.5$	Lozier et al. (2019)	
<b>2000-09 decade</b>									
A10 (2003)									
Brazil basin	45-15.3°W	Bottom	12:63	9:11	$6.9 \pm 1.8$	2.4	$4.2 \pm 1.8$	Hogg & Owens (1999)	
Vema channel	39.7-37.7°W	AABW	21:25	9:11	$4.0 \pm 0.4$	1.3	$3.8 \pm 0.4$	Hogg et al. (1982)	
Walvis R. North	7.3°W-1.7°E	Bottom	75:87	9:11	$0 \pm 1$	0.3	$-0.4 \pm 0.9$	Warren & Speer (1991)	
Walvis R. South	2.2-13.4°E	Bottom	88:106	9:11	$0 \pm 1$	1.2	$-0.8 \pm 1.3$	Warren & Speer (1991)	
Brazil current	Coast-44.8°W	Surf - interm	1:12	1:7	$-38.9 \pm 2.1$	-21.7	$-38.2 \pm 1.3$	Hernández-Guerra et al. (2019)	
Benguela current	Coast-11.8°E	Surf - interm	101:110	1:7	$26.3 \pm 2.4$	27.8	$26.3 \pm 1.5$	Hernández-Guerra et al. (2019)	
A095 (2009)									
Brazil current	Coast-38.8°W	< 300 dbar	1:4	1:4	$-4.9 \pm 1.2$	-3.1	$-3.5 \pm 0.2$	Bryden et al. (2011)	
A05 + Florida (2004)									
Florida Current	All	All	1:8	1:6	$31.9 \pm 3.3$	31.9	$32.2 \pm 0.3$	Florida Current Project	
A03 (2005)									
DWBC	Coast to 70°W	yn 27.8-28.125	1:9	7:9	$-25.1 \pm 2.7$	2.8	$-23.4 \pm 0.1$	Toole et al. (2011)	
AR07W (2005)									
Bering Strait (Davis Strait)	All	All	1:25	1:11	$-1.6 \pm 0.2$	-6.4	$-1.6 \pm 1.3$	Curry et al. (2014)	
AR07E (2007)									
Bering Strait (East)	All	All	26:66	1:11	$0.80 \pm 0.63$	0.1	$0.7 \pm 2.9$	Lozier et al. (2019)	

**2010-19 decade**

A10 (2011)								
Brazil basin	45-15.3°W	Bottom	10:65	9:11	6.9 ± 1.8	4.7	4.8 ± 1.9	Hogg & Owens (1999)
Vema channel	39.7-37.7°W	AABW	22:28	9:11	4.0 ± 0.4	2.5	3.9 ± 0.4	Hogg et al. (1982)
Walvis R. North	7.3°W-1.7°E	Bottom	76:92	9:11	0 ± 1	0.6	-0.4 ± 0.9	Warren & Speer (1991)
Walvis R. South	2.2-13.4°E	Bottom	93:116	9:11	0 ± 1	1.1	-0.8 ± 1.2	Warren & Speer (1991)
Brazil current	Coast-44.8°W	Surf - interm	1:25	1:7	-38.9 ± 2.1	-16.9	-38.4 ± 1.5	Hernández-Guerra et al. (2019)
Benguela current	Coast-11.8°E	Surf - interm	105:119	1:7	26.3 ± 2.4	39.0	26.8 ± 1.6	Hernández-Guerra et al. (2019)
A095 (2018)								
Brazil current	Coast-38.8W	< 300 dbar	1:4	1:10	-4.9 ± 1.2	-4.0	-5.2 ± 0.6	Bryden et al. (2011)
A05 + Florida (2011)								
Florida Current	All	All	1:13	1:6	31.3 ± 3.4	30.1	30.1 ± 0.2	Florida Current Project
AR07W (2014)								
Bering Strait (Davis Strait)	All	All	1:39	1:11	-1.6 ± 0.2	1.0	-1.6 ± 1.5	Curry et al. (2014)
AR07E (2014)								
Bering Strait (East)	All	All	40:141	1:11	0.80 ± 0.63	1.3	0.7 ± 2.4	Lozier et al. (2019)

## References for this Supporting Information

- Artana, C., Ferrari, R., Koenig, Z., Sennéchaël, N., Saraceno, M., Piola, A. R., & Provost, C. (2018). Malvinas current volume transport at 41°S: A 24 yearlong time series consistent with mooring data from 3 decades and satellite altimetry. *Journal of Geophysical Research: Oceans*, 123(1), 378–398. <https://doi.org/10.1002/2017JC013600>
- Bryden, H. L., King, B. A., & McCarthy, G. D. (2011). South Atlantic overturning circulation at 24°S. *Journal of Marine Research*, 69(1), 39–56. <https://doi.org/10.1357/002224011798147633>
- Caínzos, V., Hernández-Guerra, A., McCarthy, G. D., McDonagh, E. L., Cubas Armas, M., & Pérez-Hernández, M. D. (2022). Thirty Years of GOSHIP and WOCE Data: Atlantic Overturning of Mass, Heat, and Freshwater Transport. *Geophysical Research Letters*, 49(4). <https://doi.org/10.1029/2021GL096527>
- Curry, B., Lee, C. M., Petrie, B., Moritz, R. E., & Kwok, R. (2014). Multiyear volume, liquid freshwater, and sea ice transports through Davis Strait, 2004–10. *Journal of Physical Oceanography*, 44(4), 1244–1266. <https://doi.org/10.1175/jpo-d-13-0177.1>
- Drévilion, M., Bahrel, P., Bazin, D., Benkiran, M., Beuvier, J., Crosnier, L., et al. (2018). Learning about Copernicus Marine Environment Monitoring Service “CMEMS”: A Practical Introduction to the Use of the European Operational Oceanography Service. In E. Chassignet, A. Pascual, J. Tintoré, & J. Verron (Eds.), *New Frontiers in Operational Oceanography* (pp. 695–712). GODAE OceanView. <https://doi.org/10.17125/gov2018.ch25>
- Finucane, G., & Hautala, S. (2022). Transport of Antarctic Bottom Water Entering the Brazil Basin in a Planetary Geostrophic Inverse Model. *Geophysical Research Letters*, 49(22), 1–9. <https://doi.org/10.1029/2022GL100121>
- Forget, G., Campin, J.-M., Heimbach, P., Hill, C. N., Ponte, R. M., & Wunsch, C. (2015). ECCO version 4: an integrated framework for non-linear inverse modeling and global ocean state estimation. *Geoscientific Model Development*, 8(10), 3071–3104. <https://doi.org/10.5194/gmd-8-3071-2015>
- Fu, Y., Li, F., Karstensen, J., & Wang, C. (2020). A stable Atlantic Meridional Overturning Circulation in a changing North Atlantic Ocean since the 1990s. *Science Advances*, 6(48), eabc7836. <https://doi.org/10.1126/sciadv.abc7836>
- Fu, Yao, Karstensen, J., & Brandt, P. (2018). Atlantic Meridional Overturning Circulation at 14.5° N in 1989 and 2013 and 24.5° N in 1992 and 2015: volume, heat, and freshwater transports. *Ocean Science*, 14(4), 589–616. <https://doi.org/10.5194/os-14-589-2018>
- Fukumori, I., Wang, O., Fenty, I., Forget, G., Heimbach, P., & Ponte, R. M. (2017). *ECCO Version 4 Release 3*. Retrieved from <http://hdl.handle.net/1721.1/102062>
- Ganachaud, A. S. (1999). *Large scale oceanic circulation and fluxes of freshwater, heat, nutrients and oxygen*. Woods Hole, MA: Massachusetts Institute of Technology and Woods Hole Oceanographic Institution. <https://doi.org/10.1575/1912/4130>
- Ganachaud, A. S. (2003a). Error budget of inverse box models: The North Atlantic. *Journal of Atmospheric and Oceanic Technology*, 20(11), 1641–1655. [https://doi.org/10.1175/1520-0426\(2003\)020<1641:EBOIBM>2.0.CO;2](https://doi.org/10.1175/1520-0426(2003)020<1641:EBOIBM>2.0.CO;2)
- Ganachaud, A. S. (2003b). Large-scale mass transports, water mass formation, and diffusivities estimated from World Ocean Circulation Experiment (WOCE) hydrographic data. *Journal of Geophysical Research*, 108(C7). <https://doi.org/10.1029/2002jc001565>
- Hernández-Guerra, A., Pelegrí, J. L., Fraile-Nuez, E., Benítez-Barríos, V. M., Emelianov, M., Pérez-Hernández, M. D., & Vélez-Belchí, P. (2014). Meridional overturning transports at 7.5N and 24.5N in the Atlantic Ocean during 1992–93 and 2010–11. *Progress in Oceanography*, 128, 98–114. <https://doi.org/10.1016/j.pocean.2014.08.016>
- Hernández-Guerra, A., Talley, L. D., Pelegrí, J. L., Vélez-Belchí, P., Baringer, M. O., Macdonald, A. M., & McDonagh, E. L. (2019). The upper, deep, abyssal and overturning circulation in the Atlantic Ocean at 30°S in 2003 and 2011. *Progress in Oceanography*, 176(102136). <https://doi.org/10.1016/j.pocean.2019.102136>

- Hogg, N., Biscaye, P., Gardner, W., & Schmitz, W. J. (1982). On the transport and modification of Antarctic Bottom Water in the Vema Channel. *Journal of Marine Research*, 40(Supplement), 231–263.
- Hogg, N. G., & Owens, W. B. (1999). Direct measurement of the deep circulation within the Brazil Basin. *Deep Sea Research Part II: Topical Studies in Oceanography*, 46(1–2), 335–353. [https://doi.org/10.1016/S0967-0645\(98\)00097-6](https://doi.org/10.1016/S0967-0645(98)00097-6)
- Holliday, N. P., Bacon, S., Cunningham, S. A., Gary, S. F., Karstensen, J., King, B. A., et al. (2018). Subpolar North Atlantic Overturning and Gyre-Scale Circulation in the Summers of 2014 and 2016. *Journal of Geophysical Research: Oceans*, 123(7), 4538–4559. <https://doi.org/10.1029/2018JC013841>
- Lellouche, J.-M., Greiner, E., le Galloudec, O., Garric, G., Regnier, C., Drevillon, M., et al. (2018). Recent updates to the Copernicus Marine Service global ocean monitoring and forecasting real-time 1/12° high-resolution system. *Ocean Science*, 14(5), 1093–1126. <https://doi.org/10.5194/os-14-1093-2018>
- Lozier, M. S., Li, F., Bacon, S., Bahr, F., Bower, A. S., Cunningham, S. A., et al. (2019). A sea change in our view of overturning in the subpolar North Atlantic. *Science*, 363(6426), 516–521. <https://doi.org/10.1126/science.aau6592>
- McDonagh, E. L., & King, B. A. (2005). Oceanic fluxes in the South Atlantic. *Journal of Physical Oceanography*, 35(1), 109–122. <https://doi.org/10.1175/JPO-2666.1>
- McDonagh, E. L., King, B. A., Bryden, H. L., Courtois, P., Szuts, Z., Baringer, M. O., et al. (2015). Continuous estimate of Atlantic oceanic freshwater flux at 26.5°N. *Journal of Climate*, 28, 8888–8906.
- McDonagh, Elaine L., Bryden, H. L., King, B. A., & Sanders, R. J. (2008). The circulation of the Indian Ocean at 32°S. *Progress in Oceanography*, 79(1), 20–36. <https://doi.org/10.1016/j.pocean.2008.07.001>
- McDonagh, Elaine L., McLeod, P., King, B. A., Bryden, H. L., & Valdés, S. T. (2010). Circulation, Heat, and Freshwater Transport at 36°N in the Atlantic. *Journal of Physical Oceanography*, 40(12), 2661–2678. <https://doi.org/10.1175/2010JPO4176.1>
- Robbins, P. E., & Toole, J. M. (1997). The dissolved silica budget as a constraint on the meridional overturning circulation of the Indian Ocean. *Deep Sea Research Part I: Oceanographic Research Papers*, 44(5), 879–906. [https://doi.org/10.1016/S0967-0637\(96\)00126-4](https://doi.org/10.1016/S0967-0637(96)00126-4)
- Speer, K. G., Holfort, J., Reynaud, T., & Siedler, G. (1996). South Atlantic Heat Transport at 11°S. In *The South Atlantic: present and past circulation* (pp. 105–120).
- Warren, B. A., & Speer, K. G. (1991). Deep circulation in the eastern South Atlantic Ocean. *Deep Sea Research Part A. Oceanographic Research Papers*, 38(Supplement I), S281–S322. [https://doi.org/10.1016/s0198-0149\(12\)80014-8](https://doi.org/10.1016/s0198-0149(12)80014-8)
- Wunsch, C. (1996). *The Ocean Circulation Inverse Problem*. Cambridge, USA: Cambridge University Press.